Applied Catalysis B: Environment and Energy 350 (2024) 123890

Contents lists available at ScienceDirect

Applied Catalysis B: Environment and Energy

journal homepage: www.elsevier.com/locate/apcatb

The single atomic Pt promoted CoMo heterostructure catalyst for efficient sorbitol hydrogenolysis to ethanol

Jiacheng Ji [a], Honglin Zhuang [a], Ling Zhou [b,*], Yi Zhang [a,b,**]

[a] College of Chemical Engineering, Beijing University of Chemical Technology, Beijing 100029, China

[b] Modern Agricultural Engineering Key Laboratory at Universities of Education Department of Xinjiang Uygur Autonomous Region, Tarim University, Alar, Xinjiang Uygur Autonomous Region 843300, China

ARTICLE INFO

Keywords:
Hydrogenolysis
Ethanol
Platinum
Sorbitol
Fixed-bed reactor

ABSTRACT

Ethanol (EtOH) is recognized as one of the most crucial biofuels, but the low efficiency and complex bioconversion process limit its commercial utilization. In this study, we design a single atomic Pt promoted CoMo heterostructure catalyst for ethanol synthesis from sorbitol, one of the important biochemical platforms, via a continuous-flow fixed-bed reactor. The $Pt_1/CoMoO_4$ catalyst exhibited the best catalytic performance with 99.6% sorbitol conversion and 71.6% EtOH selectivity over a 30 h reaction. A combination of Raman, XPS, XANES, EXAFS, Py-FTIR, and operando EG-DRIFTS provides insight into the synergistic effects between Co^0 and Mo^{5+} active sites during sorbitol hydrogenolysis to EtOH over $Pt_1/CoMoO_4$ catalyst. Additionally, it is discovered that the Pt_1 single atom promoter activates hydrogen and tunes the electronic properties of Co and Mo species, resulting in forming the highest content of Co^0 and Mo^{5+} active sites with higher stability and promoting the sorbitol hydrogenolysis to EtOH. This work demonstrates the validity of designing efficient catalysts with synergistic multi-active sites. Those are modulated by single atom Pt promoter, for highly selective hydrogenolysis of biomass platforms to highly value-added products.

1. Introduction

Primed by widespread concerns about fossil fuel scarcity and carbon dioxide emission restrictions, renewable biomass is widely regarded as one of the most promising alternatives for synthesizing chemicals [1]. Especially, bioethanol is universally applied as an alternative gasoline additive, which makes a contribution to energy and environmental sustainability [2]. However, the economically feasible production of bioethanol faces great challenges due to the low-efficiency process of bioconversion [3]. Therefore, the efficient chem-catalyst for converting biomass to ethanol (EtOH) is attractive to realizing sustainable development.

Sorbitol, one of the important platform biochemicals, has been attracting tremendous interest to be converted to value-added products due to its better solubility and stability compared to cellulose and glucose [4]. In previous studies, the most widely accepted mechanism for the sorbitol hydrogenolysis tandem process based on the first activation of sorbitol, subsequently followed by the retro-aldol condensation (RAC) reaction to C_2-C_4 intermediates over acid active sites and further hydrogenolysis/hydrogenation to ethylene glycol, propanediol, ethanol, etc over the hydrogenation active sites. [5,6]. In our previous works, the synergistic hydrogenolysis catalysts with tunable acidity, Ru-W/SiO_2 catalysts, were designed to convert glucose into lower diols, where the synergistic effects of metal active sites and acid sites were established to effectively catalyze the selective hydrogenolysis of the C-C and C-O bonds with hydrogenation reaction [7,8]. Besides, in order to obtain high butanediol selectivity via glucose hydrogenolysis, the special nanosheet structure of the catalysts was designed, which achieved a balance between the hydrogenation active sites and acid sites via suitable reducibility [9]. Whereas, converting sorbitol to ethanol with high selectivity remains a great challenge in the design of efficient catalysts. On one hand, because there are too many reaction steps involved in the hydrogenolysis of sorbitol to EtOH, there is a large variety of possible by-products. On the other hand, the influence of solid acid catalysts with tunable acidity on the hydrogenolysis of sorbitol is still insufficient, which affects the establishment of efficient synergistic interactions between the acidic and hydrogenation active sites and leads to the unsatisfying EtOH selectivity. For the selective hydrogenolysis of

* Corresponding author.
** Corresponding author at: College of Chemical Engineering, Beijing University of Chemical Technology, Beijing 100029, China.
E-mail addresses: zhoul-007@163.com (L. Zhou), yizhang@mail.buct.edu.cn (Y. Zhang).

https://doi.org/10.1016/j.apcatb.2024.123890
Received 20 December 2023; Received in revised form 6 February 2024; Accepted 26 February 2024
Available online 1 March 2024

sorbitol, it is believed the synergistic effect of the metal active sites and acid sites can also be known as the key to realizing outstanding sorbitol conversion with high selectivity of target production [5].

Therefore, it is essential to develop synergistic effects of hydrogenation active sites and acid sites. It is reported that the Mo-based catalysts were employed as Lewis acid sites (LASs) for hydrogenolysis C-O bonds and C-C bonds [10,11]. Furthermore, Mo^{5+} species can serve as LAS for cleaving the C-O of anisole, and the constructed Ru-Mo interfaces facilitate selective hydrogenolysis with the Ru^0 cooperation [12]. Additionally, LAS is widely recognized as the key to promoting RAC reaction for cleaving the C-C bonds [11,12]. Simultaneously, Co^0 displayed a great ability to facilitate H_2 activation [13,14]. Meanwhile, Ding et al. found that Co-doped MoO_2/CNT displays a higher catalytic activity and satisfactory stability in the hydrogenolysis of phenol due to changing the electronic properties of the adjacent Mo atoms when Co species doped [15]. Therefore, it is reasonable to design CoMo heterostructure catalysts which can simultaneously expose Co metal active sites and LAS for selective hydrogenolysis of sorbitol to ethanol.

Besides, single atom catalysts have attracted considerable research interest due to their maximum atom efficiency and unique electronic properties [16–18]. Park et al. found that the Pt SA/WO_{3-x} catalyst has a higher degree of hydrogen spillover effect compared to the Pt NP/WO_{3-x} catalyst [19], which significantly contributes to maintaining the metallic hydrogenation active sites. Moreover, regarding the catalytic performance, the addition of single atom species can modulate the electron transfer to improve the stability of catalysts [20]. Therefore, it is reasonable to employ Pt_1 single atom as a promoter to tune the synergistic effects of hydrogenation active sites and acid sites.

Despite the significant efforts dedicated to sorbitol hydrogenolysis processes, it is still necessary to figure out a clear picture of multiple active sites during the reaction. In this work, we designed the CoMo heterostructure catalysts ($Pt_1/CoMoO_4$, $CoMoO_4$, 17Co-MoO_3, and Co&Mo Mixed) with the similar Co: Mo surface molar ratio (45: 55) prepared by different methods to establish the synergistic effects of metal active sites and LASs for selective hydrogenolysis of sorbitol to EtOH via a continuous-flow fixed bed reactor. The obtained catalysts were investigated by various characterization, including Raman, XPS, XANES, EXAFS, Py-FTIR, and operando EG-DRIFTS, to explore the synergistic effects of metal active sites and LASs on CoMo heterostructure catalysts.

2. Experimental

2.1. Reagents and materials

Cobalt (II) acetate tetrahydrate ($Co(CH_3COO)_2{\cdot}4\ H_2O$, ≥ 99.0%), Ammonium molybdate (VI) tetrahydrate ($(NH_4)_6Mo_7O_{24}){\cdot}4\ H_2O$, ≥ 99.0%), Cobaltous (II) nitrate hexahydrate ($Co(NO_3)_2{\cdot}6\ H_2O$, ≥ 99.0%), Tricobalt tetroxide (Co_3O_4, ≥ 99.0%), Molybdenum (VI) oxide (MoO_3, ≥99.0%), Ethanol (EtOH, ≥ 99.0%) was purchased from Beijing Chemical Corp. Diamminedinitritoplatinum solution ($Pt(NO_2)_2(NH_3)_2$, 3.4 wt% in dilute ammonium hydroxide) was purchased from Sigma-Aldrich, Co.

2.2. Catalysts preparation

The $CoMoO_4$ precursor was prepared by the coprecipitation method. $Co(CH_3COO)_2{\cdot}4\ H_2O$ and $(NH_4)_6Mo_7O_{24}{\cdot}4\ H_2O$ were dissolved into 200 mL of deionized water under vigorous stirring at 85 °C for 4 h. After separating the precipitation from the system by suction filtration, the precipitation was washed with deionized water and ethanol for several times. Subsequently, the precipitation was dried at 80 °C for 12 h and then calcinated at 500 °C for 3 h.

The $Pt_1/CoMoO_4$ catalyst was prepared by impregnation method on the $CoMoO_4$ precursor. Firstly, the $CoMoO_4$ precursor was impregnated with the aqueous solution of $Pt(NO_2)_2(NH_3)_2$. The Pt loading of $Pt_1/CoMoO_4$ was set as 0.1 wt%. Then the sample was dried at 120 °C for 12 h. After that, the sample was calcinated at 400 °C for 2 h.

The 17Co-MoO_3 catalyst was also prepared by the impregnation method. In order to keep the Co: Mo surface molar ratio 45: 55, we set the Co loading of 17 wt%. MoO_3 was dried at 120 ℃ for 12 h before being impregnated with an aqueous solution of $Co(NO_3)_2$. Then the sample was dried at 120 ℃ overnight and calcinated at 400 ℃ for 2 h.

The Co&Mo Mixed catalyst was prepared by a physical mixing approach. Co_3O_4 and MoO_3 (mole ratio=1:3) were ground in mortar for 20 min. Then, all the samples were pressed into pellets (18 MPa), crushed, and sieved to retain 20–40 mesh particles for reaction tests.

2.3. Catalysts characterization

N_2 adsorption-desorption isotherms were analyzed on Micromeritics ASAP 2020 equipment (Micromeritics, USA). The pore properties were analyzed by the BJH method. Before the measurement, samples were degassed at 180 ℃ for 6 h under vacuum. Powder X-ray diffraction (XRD) patterns of fresh reduced and passivated catalysts were detected on Ultima IV equipped with Cu Kα radiation (λ=0.154 nm) at a scanning rate of 5° min^{-1} from 15 to 80°at 3 KW. Raman spectra of the catalysts were recorded with a HORIBA Scientific LabRAM HR Evolution using the 514 nm argon ion laser.

Scanning electron microscopy (SEM) equipped with an energy-dispersive X-ray (EDX) detector. High-resolution transmission electron microscopy (HR-TEM) images were conducted by a JEM-3010 high-resolution transmission electron microscopy operating after the samples were prepared by ultrasonic dispersion in the ethanol and dropped on the Ultra-thin carbon film grids. High-angle annular dark-field scanning transmission electron microscopy (HAADF-STEM) was performed on a JEM F200 microscope.

H_2 temperature-programmed reduction (H_2-TPR) profiles were carried out on a FINESORB 3010 H equipped with a thermal conductivity detector (TCD). 0.1 g of fresh catalysts were packed inside the quartz tube. The reducing gas, 10% H_2 mixed with Ar, was brought into the reactor at a rate of 30 mL/min. And the samples were reduced by 10 ℃/min from 50 to 650 ℃. NH_3 temperature programmed desorption (NH_3-TPD) measurements were performed on Autosorb-iQ-C (Quantachrome, USA). The samples were pretreated at 245 ℃ for 1 h in 10% H_2 flow. After purged by N_2 at 50 ℃, ammonia was introduced into the reactor and kept for 30 min at 50 ℃. Subsequently, the desorption profiles from 50 to 600 ℃ were obtained at a ramping rate of 10 ℃/min with the N_2 flow after the physical adsorption of NH_3 was removed by N_2. The effluent gas composition was analyzed by a downstream gas chromatograph equipped with TCD.

X-ray photoelectron spectra (XPS) was measured on a Thermo Scientific K-Alpha+ instrument equipped with a monochromatic Al Kα. Co K-edge, Mo K-edge, and Pt L-edge X-ray absorption fine structure spectra were tested at the BL11B Beamline at Shanghai Synchrotron Radiation Facility (SSRF, Shanghai, China). The data of Co K-edge and Mo K-edge were tested in transmission mode, and the data of Pt L-edge were tested in fluorescence mode. The X-ray energy was calibrated by standard Mo, Co, and Pt metal foil. The spectra were processed and analyzed by the software codes Athena and Artemis [21].

The Pyridine-Fourier Transform Infrared spectroscopy (Py-FTIR) was recorded on a Nicolet 5700 FTIR spectrometer (resolution 4 cm^{-1}) equipped with a mercury cadmium telluride (MCT) detector. The samples were placed in an infrared cell with a ZnSe window and reduced for 1 h in H_2 flow at 245 ℃ at atmospheric pressure. After that, N_2 was introduced into the cell to purge for 0.5 h. Subsequently, pyridine was brought into the cell at 50 ℃ as the probe molecule. Then, N_2 flow was brought into the cell to remove the physically adsorbed probe molecule to record the chem-adsorbed probe molecule over the surface of the samples.

The operando EG diffuse reflectance infrared Fourier transform spectrum (operando EG- DRIFTS) was collected on a Thermo Scientific

Table 1
Sorbitol conversion and product distribution of different CoMo heterostructure catalysts. [a, b].

Catalysts	Con. / %	Sel. / %[c]						
		GLY	EG	1,2-PDO	1,3-PDO	1,2-BDO	EtOH	Others
$Pt_1/CoMoO_4$	99.6	4.7	4.7	10.9	1.4	3.2	71.6	3.5
$CoMoO_4$	89.8	5.7	19.4	12.4	1.5	3.5	54.2	3.3
17Co-MoO_3	67.4	5.0	9.2	15.6	3.0	3.0	60.0	4.2
Co&Mo Mixed	100.0	9.0	13.2	28.2	3.1	4.0	34.7	7.8

a: Reaction conditions: 0.5 g catalysts, 5 MPa H_2, 245 ℃, 5 wt% Sorbitol aqueous solution, GHSV(H_2) = 8400 cm^3 g_{cat}^{-1} h^{-1}, LHSV (5 wt% Sor. aqueous solution) = 6 cm^3 g_{cat}^{-1} h^{-1}.
b: The data of $CoMoO_4$, 17Co-MoO_3, and Co&Mo Mixed catalysts were collected at the 20th hour of time on stream, and calculated based on the mole percent. The data of the $Pt_1/CoMoO_4$ catalyst was collected after the long-term reaction (30 hours).
c: GLY = Glycerol, EG = Ethylene Glycol, 1,2-PDO = 1,2-Propanediol, 1,3-PDO = 1,3-Propanediol, 1,2-BDO = 1,2-Butanediol, EtOH = Ethanol, Others: Gas products of CH_4 and C_2H_6, liquid products of Butanetriol, Propanol etc.

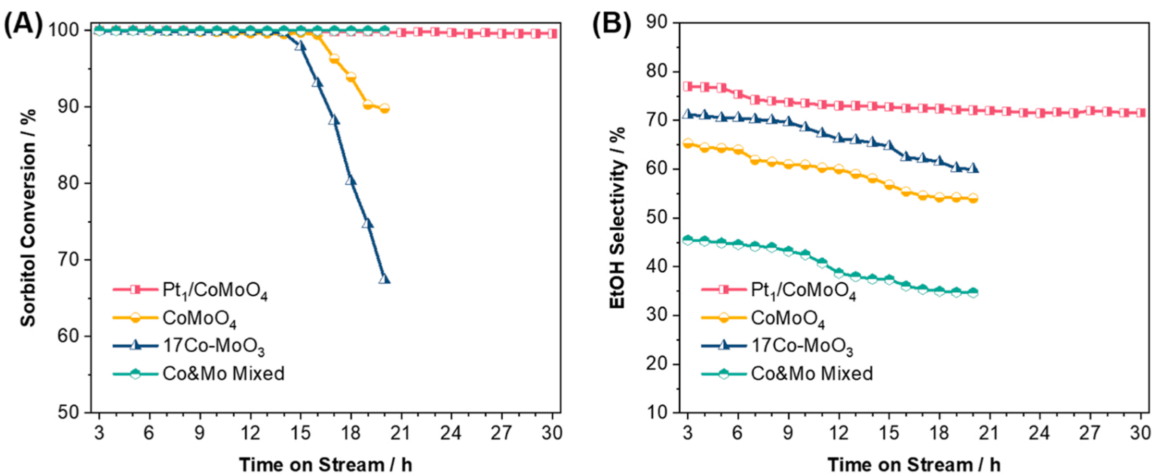

Fig. 1. Reaction performance of various catalysts. (A) Sorbitol conversion of the various catalysts, (B) EtOH selectivity of the various catalysts. Reaction conditions: 0.5 g catalysts, 5 MPa H_2, 245 ℃, 5 wt% sorbitol aqueous solution, GHSV(H_2) = 8400 cm^3 g_{cat}^{-1} h^{-1}, LHSV (5 wt% Sor. aqueous solution) = 6 cm^3 g_{cat}^{-1} h^{-1}.

Nicolet iS50 FTIR spectrometer (resolution 4 cm^{-1}) equipped with a mercury cadmium telluride (MCT) detector. After pretreated by H_2 flow for 1 h and purged by N_2 at 50 ℃ 1 h, EG carried by N_2 was brought into the cell for 1 h at 245 ℃. Subsequently, H_2 was brought into the cell at the same temperature to detect the reaction between H_2 and EG.

2.4. Catalysts evaluation test

0.5 g catalysts (20–40 mesh) were loaded in the middle of the fixed bed stainless steel reactor and fixed by quartz wood. The reaction temperature of the catalyst bed was monitored by a K-type thermocouple controlled by a PID controller. The sorbitol hydrogenolysis reactions were carried out in a continuous flow at 245 ℃, 5 MPa H_2, GHSV(H_2) = 8400 $cm^3 \cdot g^{-1} \cdot h^{-1}$, LHSV = 6 $cm^3 \cdot g^{-1} \cdot h^{-1}$. The liquid feed (5 wt%) was introduced to flowing gas streams using a liquid infusion pump (LC-20AT, Shimadzu). Before the reaction, the catalyst was pre-reduced by H_2 at 350 ℃ for 10 h in situ at atmospheric pressure with GHSV (H_2) =9600 $cm^3 \cdot g^{-1} \cdot h^{-1}$. The effluent gas was online analyzed by gas chromatography (GC-2014 C, Shimadzu) equipped with a thermal conductivity detector (TCD). During the reaction, the liquid-phase product was separated from the reaction system each hour and analyzed by high-performance liquid chromatography (HPLC) Waters 2695 instrument with a refractive index detector (RID) (Waters 2414, RI detector). And the separate steps were completed by an HPX-87 H column (BIO-RAD). The mobile phase was 5 mM H_2SO_4 with a flow rate of 0.6 mL/min. The temperature of the column and detector was 50 °C.

The sorbitol conversion was calculated on a carbon-mole basis, as follows:

$$\text{Sor. Conv.} = \{(\text{Sor}_{\text{inlet}} - \text{Sor}_{\text{outlet}}) / \text{Sor}_{\text{inlet}}\} \times 100\% \tag{1}$$

The selectivity of the polyol product was calculated based on the mole selectivity and obtained according to Eq. (2):

$$S = \{N_{CxHyOz} / \sum N_{CxHyOz}\} \times 100\% \tag{2}$$

N_{CxHyOz} indicated the molar number toward a product with x carbon atoms.

The carbon balance was calculated as follows:

$$\text{Carbon Balance} = \{\sum (N_{CxHyOz} \times x)/N_{Sor} \times 6\} \times 100\% \tag{3}$$

N_{CxHyOz} indicated the molar number toward a product with x carbon atoms.

N_{Sor} indicated the molar number of the converted sorbitol.

The carbon balance of the Co-Mo catalysts with different integrating methods is above 95%.

3. Results and discussion

3.1. The catalytic performance in sorbitol hydrogenolysis reaction

The reaction results of sorbitol hydrogenolysis over the various CoMo heterostructure catalysts with the similar Co: Mo surface molar ratio (Table S1) are summarized in Table 1 and Fig. 1. The major products are EtOH, EG, and 1,2-PDO over all catalysts. As illustrated in Fig. 1A, the $Pt_1/CoMoO_4$ catalyst performs excellent stability within 30 h with near 100% sorbitol conversion. However, the $CoMoO_4$ and 17Co-MoO_3 catalysts deactivate at 16 and 14 h, respectively. Meanwhile, the Co&Mo Mixed catalyst performs in a distinct way with 100% sorbitol conversion but the lowest EtOH selectivity (34.7%).

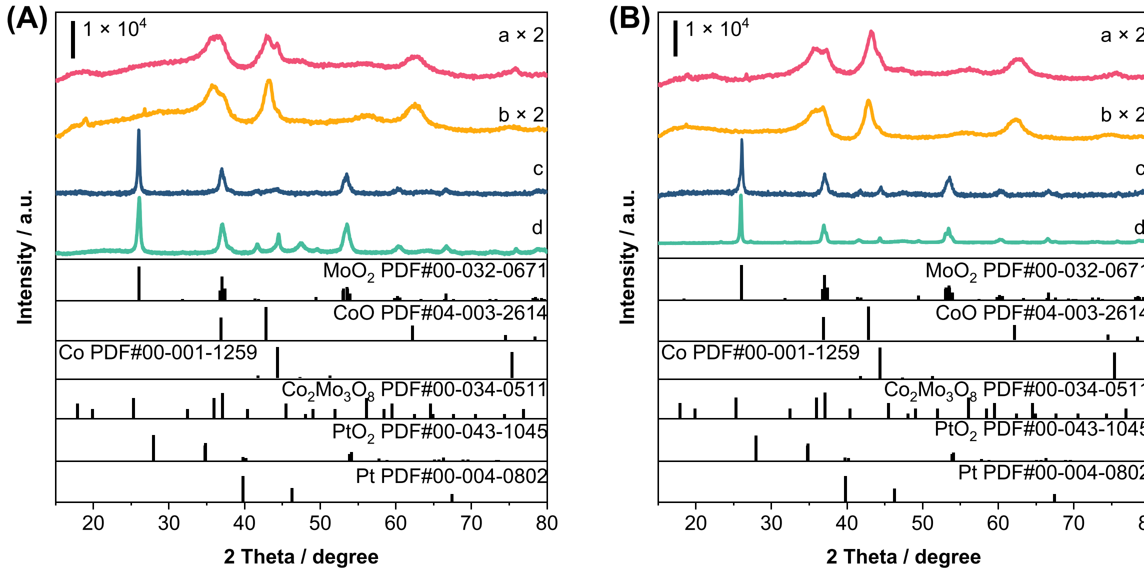

Fig. 2. XRD patterns of various CoMo heterostructure catalysts. (A) the samples of the initial states (2nd hour); (B). the samples of the steady states (20th hour). The $Pt_1/CoMoO_4$ (a) was the sample of the 30th hour. (a) $Pt_1/CoMoO_4$, (b) $CoMoO_4$, (c) 17Co-MoO_3, and (d) Co&Mo Mixed.

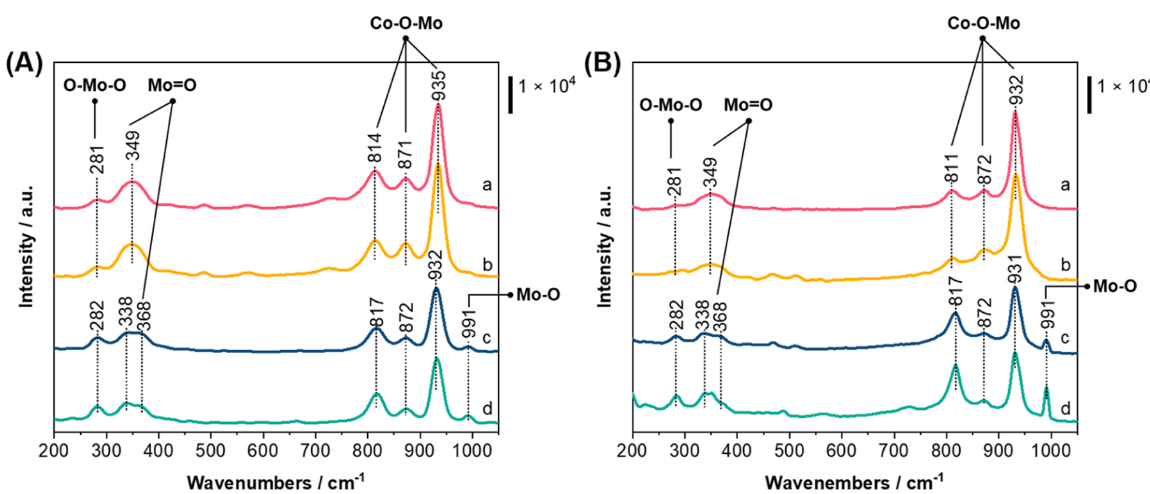

Fig. 3. Raman spectra of various CoMo heterostructure catalysts. (A). the samples of the initial states (2nd hour); (B). the samples of steady state (20th hour). The $Pt_1/CoMoO_4$ (a) was the sample of the 30th hour. (a) $Pt_1/CoMoO_4$, (b) $CoMoO_4$, (c) 17Co-MoO_3, and (d) Co&Mo Mixed.

Remarkably, as compared in Table 1 and Fig. 1B, the $Pt_1/CoMoO_4$ catalyst shows 71.6% EtOH selectivity after the 30 hours reaction with the greatest stability, demonstrating the added Pt_1 single atom promotes the sorbitol hydrogenolysis to EtOH. Besides, as listed in Table S2, comparing to the reported hydrogenolysis of cellulose, sorbitol, and glucose to ethanol, the best yield and STY of EtOH are obtained by $Pt_1/CoMoO_4$ catalyst via continuous-flow fixed bed reactor in this work.

As previous studies found, the formation of EtOH is dominated by EG hydrogenolysis for cleaving C-O bonds with active hydrogen [3,22], suggesting that the added small amount of Pt_1 promoter greatly contributes to forming the active sites for selectively cleaving the C-O bonds of EG on the $Pt_1/CoMoO_4$ catalyst. For the 17Co-MoO_3 and $CoMoO_4$ catalysts, different preparation method leads to distinct surface chemical states of Co and Mo species which might promote the competitive product generation, such as EG and PDO. Thus, the lower EtOH selectivity was obtained over these catalysts (54.2% for the $CoMoO_4$, and 60.0% for the 17Co-MoO_3 catalysts). On the other hand, the Co&Mo Mixed catalyst has the highest PDO selectivity (31.3%) with the lowest EtOH selectivity (34.7%). It indicates that the different preparation method makes an impact on the formation of various active sites due to the modulated surface chemical states of Co and Mo species.

Interestingly, as exhibited in Fig. 1, it is worth noting that except for the Pt_1CoMoO_4 catalyst, the EtOH selectivity dynamically decreases with time on stream for all catalysts. These suggest that the surface chemical states of catalysts are dynamically modified during the hydrogenolysis reaction via a continuous-flow fixed bed reactor. Therefore, in order to reveal the various active sites and the structure-performance relationship of the different CoMo heterostructure catalysts for sorbitol hydrogenolysis, the obtained catalysts of initial (the 2nd hour of the time on reaction stream) and steady (the last hour of time on reaction stream) states were characterized by various methods.

3.2. Characterization

3.2.1. Morphology of various catalysts

The XRD patterns of the different fresh CoMo heterostructure catalysts are exhibited in Fig. S1A. The diffractogram of the fresh $CoMoO_4$ and $Pt_1/CoMoO_4$ samples shows the specific peaks associated with the $CoMoO_4$ phase (PDF#73–1331). Meanwhile, no diffraction peaks of Pt species are observed for the $Pt_1/CoMoO_4$ sample, suggesting the highly

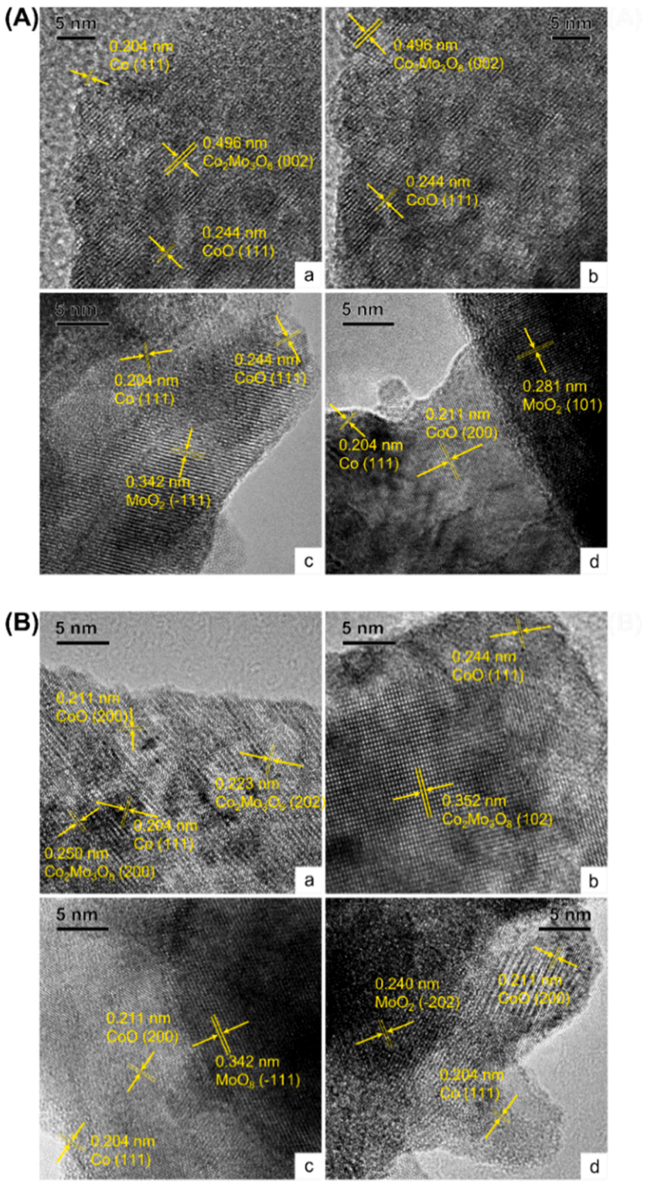

Fig. 4. HR-TEM of various CoMo heterostructure catalysts. (A). the samples of the initial states (2nd hour); (B). the samples of steady state (20th hour). The $Pt_1/CoMoO_4$ (a) was the sample of the 30th hour. (a) $Pt_1/CoMoO_4$, (b) $CoMoO_4$, (c) 17Co-MoO_3, and (d) Co&Mo Mixed.

dispersed Pt because of the low loading. Additionally, the diffractogram of the fresh 17Co-MoO_3 and Co&Mo Mixed sample exhibits the MoO_3 phase (PDF#76–1003) dominantly, and the Co_3O_4 phase (PDF#43–1003) is also observed. The weaker diffraction peak intensity of Co_3O_4 in the 17Co-MoO_3 catalyst is indicative of the highly dispersed Co species on the MoO_3 surface. In detail, for the 17Co-MoO_3, the tiny diffraction peaks at $2\theta = 24.8°$ and $28.8°$ are ascribed to the $CoMoO_4$ phase formed during the calcination process [23]. N_2 adsorption-desorption results of all catalysts (Fig. S2) exhibit the typical type-II N_2 sorption isotherm assigned to non-porosity catalysts with low specific surface area (Table S1), which can avoid the diffusion limitation in the multiphase reaction system [24].

As shown in Fig, 2 A, the XRD patterns of the various samples in the initial states exhibit the diffraction peaks of $Co_2Mo_3O_8$, CoO, and metallic Co phase on the $CoMoO_4$ and $Pt_1/CoMoO_4$ samples [25]. And, the diffractogram of the 17Co-MoO_3 and Co&Mo Mixed sample in the initial state exhibits the MoO_2 phase dominantly. Therefore, it suggests that more content of $CoMoO_x$ formed over the $CoMoO_4$ and $Pt_1/CoMoO_4$

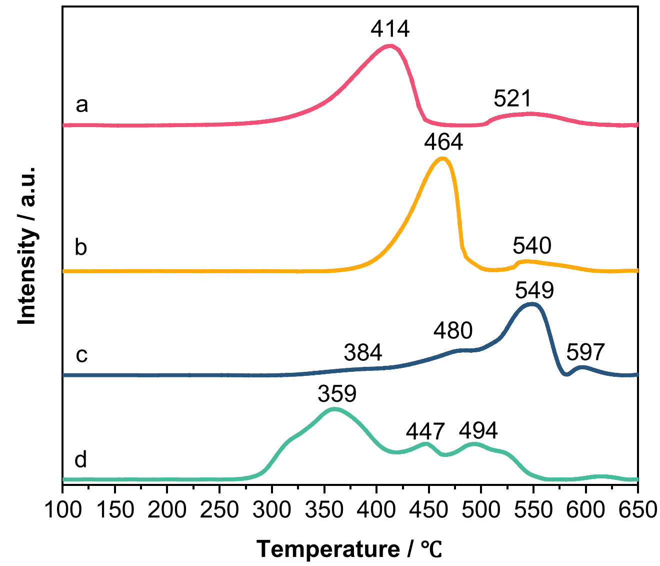

Fig. 5. H_2-TPR profiles of the Co-Mo catalysts with different integration modes. (a) $Pt_1/CoMoO_4$, (b) $CoMoO_4$, (c) 17Co-MoO_3, and (d) Co&Mo Mixed.

catalysts, which was known as LAS to adsorb and activate the C-O bonds [26,27]. On the other hand, the LAS is also recognized as the active site for selectively cleaving C-C bonds via Retro-aldol condensation during sorbitol or glucose hydrogenolysis [7,28]. Additionally, the $Pt_1/CoMoO_4$ and Co&Mo Mixed samples in the initial state show a stronger intensity of metallic Co diffraction peaks. Notably, Co^0 species are known as the active sites for facilitating H_2 dissociation, which is essential for hydrogenolysis EG intermediates to EtOH with the cooperation of LAS [29].

Furthermore, the XRD of the samples in the steady state is displayed in Fig. 2B. Compared to $CoMoO_4$, the $Pt_1/CoMoO_4$ displays a higher intensity of Co^0, suggesting that the added Pt promoter contributes to generating Co^0 species, keeping these sites more stable, and resulting in the higher stability for hydrogenolysis sorbitol with higher EtOH selectivity [29].

Fig. S1B shows the enlarged region of the metallic Co phase in the XRD patterns of 17Co-MoO_3 and Co&Mo Mixed catalysts. For the 17Co-MoO_3 catalysts, the narrower diffraction peak of metallic Co is shown in the steady states compared to that in the initial state. This indicates that Co^0 is aggregated on the surface of the 17Co-MoO_3 catalyst with the time on stream of the reaction, which is responsible for its deactivation [30].

The Raman spectra of various used catalysts in initial and steady states were detected to reveal the dynamic transformation of the active sites with the time on the reaction stream.

As shown in Fig. 3A, the bands at ~814, 871, and 935 cm^{-1} should be attributed to the stretching of Co-O-Mo modes for the initial $CoMoO_4$ and $Pt_1/CoMoO_4$ catalysts [31], those display higher intensity than that of 17Co-MoO_3 and Co&Mo Mixed catalysts, suggesting more Co-Mo interaction sites on the $CoMoO_4$ and $Pt_1/CoMoO_4$ catalysts. And the bands located at 281 and 349 cm^{-1} are assigned to the O-Mo-O bending vibration and the Mo═O twist [32]. For the 17Co-MoO_3 and Co&Mo Mixed catalysts, the bands at 338, and 368 cm^{-1} are attributed to the Mo═O twist of MoO_x and $CoMoO_x$, respectively [32,33]. Besides, the bands at 991 cm^{-1} could be noticed with respect to the MoO_3 species [34], those cannot be found in the $CoMoO_4$ and $Pt_1/CoMoO_4$ Raman spectra, suggesting there are more Co-Mo interaction sites on the $CoMoO_4$ and $Pt_1/CoMoO_4$ catalysts.

Furthermore, as shown in Fig. 3B, the sharper bands of the Mo═O of MoO_3 can be noticed at 991 cm^{-1} for the steady 17Co-MoO_3 and Co&Mo Mixed catalysts, indicating that more MoO_3 formed during the reaction due to the weakened Co-Mo interaction [34]. On the contrary, for the steady $CoMoO_4$ and $Pt_1/CoMoO_4$ catalysts, there is still no band

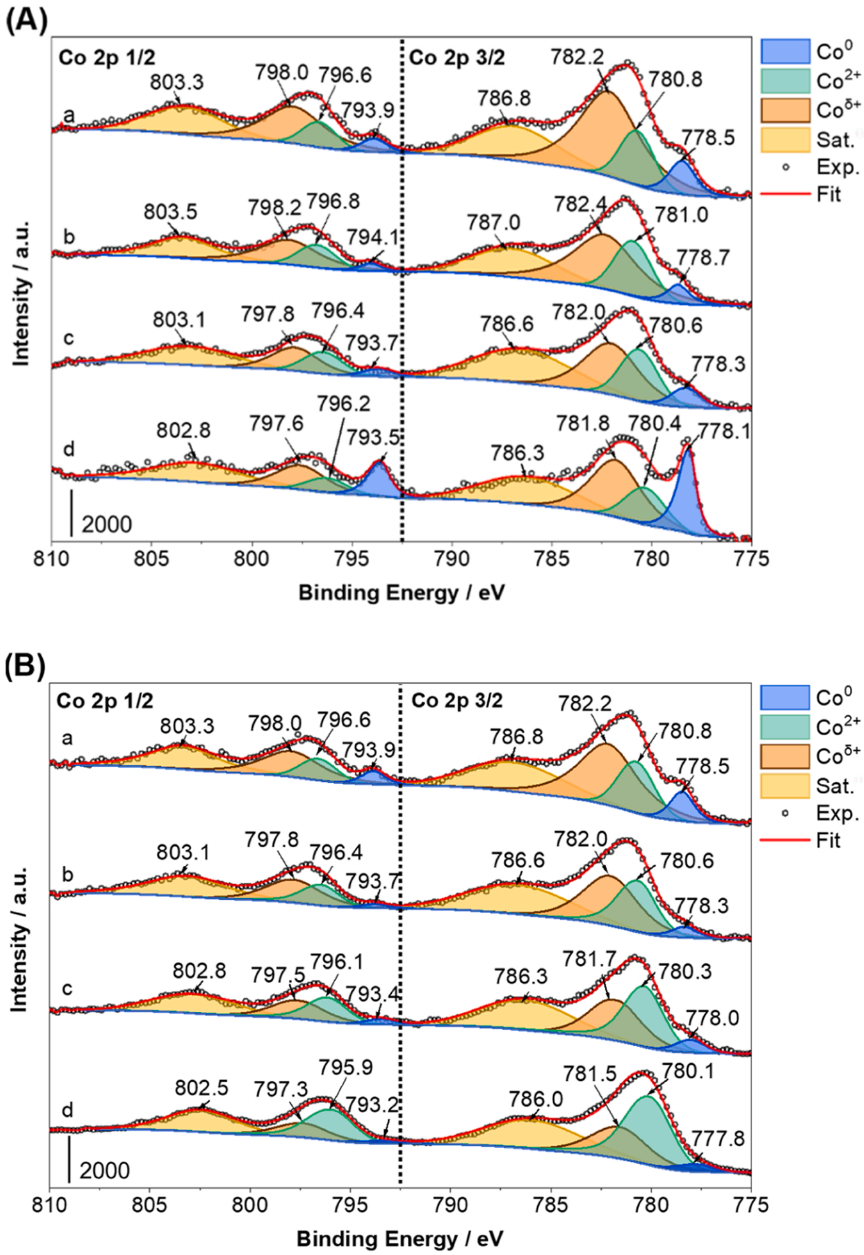

Fig. 6. XPS results of Co 2p for the different Co-Mo catalysts in the (A) initial state (2nd hour) and (B) steady state (20th hour). The $Pt_1/CoMoO_4$ (a) was the sample of the 30th hour. (a) $Pt_1/CoMoO_4$, (b) $CoMoO_4$, (c) 17Co-MoO_3, and (d) Co&Mo Mixed.

attributed to MoO_3 (at ~991 cm^{-1}) can be found, demonstrating the higher stability compared to the 17Co-MoO_3 and Co&Mo Mixed catalysts. With the time on stream of the reaction, the band of Mo=O displays a slight shift from 935 to 932 cm^{-1} with the decreased intensity, implying the Co-Mo interaction is slightly weakened [31]. Moreover, the band intensity of Co-O-Mo mode of $Pt_1/CoMoO_4$ and $CoMoO_4$ is much higher than that of 17Co-MoO_3 and Co&Mo Mixed catalysts, suggesting that the more Co-Mo interaction sites were preserved on $Pt_1/CoMoO_4$ and $CoMoO_4$. As previously reported, the interaction between Co and Mo endows the catalysts with Lewis acidity, which contributes to cleaving C-C bonds for hydrogenolysis sorbitol [7,28]. It can be known as the reason for the higher C_2 (EG + EtOH) selectivity obtained on $CoMoO_4$ and $Pt_1/CoMoO_4$ catalysts.

From the HR-TEM images of the catalysts in the initial and steady states, $Co_2Mo_3O_8$, CoO, Co, and MoO_x are observed as shown in Fig. 4, which is in line with the results of XRD and Raman. It can be observed that more CoO species are generated on the $CoMoO_4$ catalyst with the time on stream of the reaction, which can be the reason for the EtOH selectivity decline. However, the added Pt_1 single atom promoter effectively inhibits this transform, which leads to the higher content of $CoMoO_x$ and Co^0 species for hydrogenolysis sorbitol to EtOH.

SEM, HAADF-STEM, and EDS of the various catalysts in the initial states are shown in Fig. S3A and S4A. The $CoMoO_4$ and $Pt_1/CoMoO_4$ catalysts show very similar morphology, with the homogeneous distribution of Co and Mo elements as shown in the EDS elemental mapping. Additionally, SEM, HAADF-STEM, and EDS of the catalysts in the steady states are also detected (Fig. S3B and S4B). And the morphology is preserved with the time on stream of the reaction for the $CoMoO_4$ and $Pt_1/CoMoO_4$ samples, contributing to the good stability during the hydrogenolysis reaction. However, for the EDS of the 17Co-MoO_3 catalyst in the steady state (Fig. S3 and S4B), the Co species display an aggregation trend, which can be known as the reason for the deactivation in the sorbitol hydrogenolysis [30].

Meanwhile, combined with the XRD, Raman, SEM, and HR-TEM

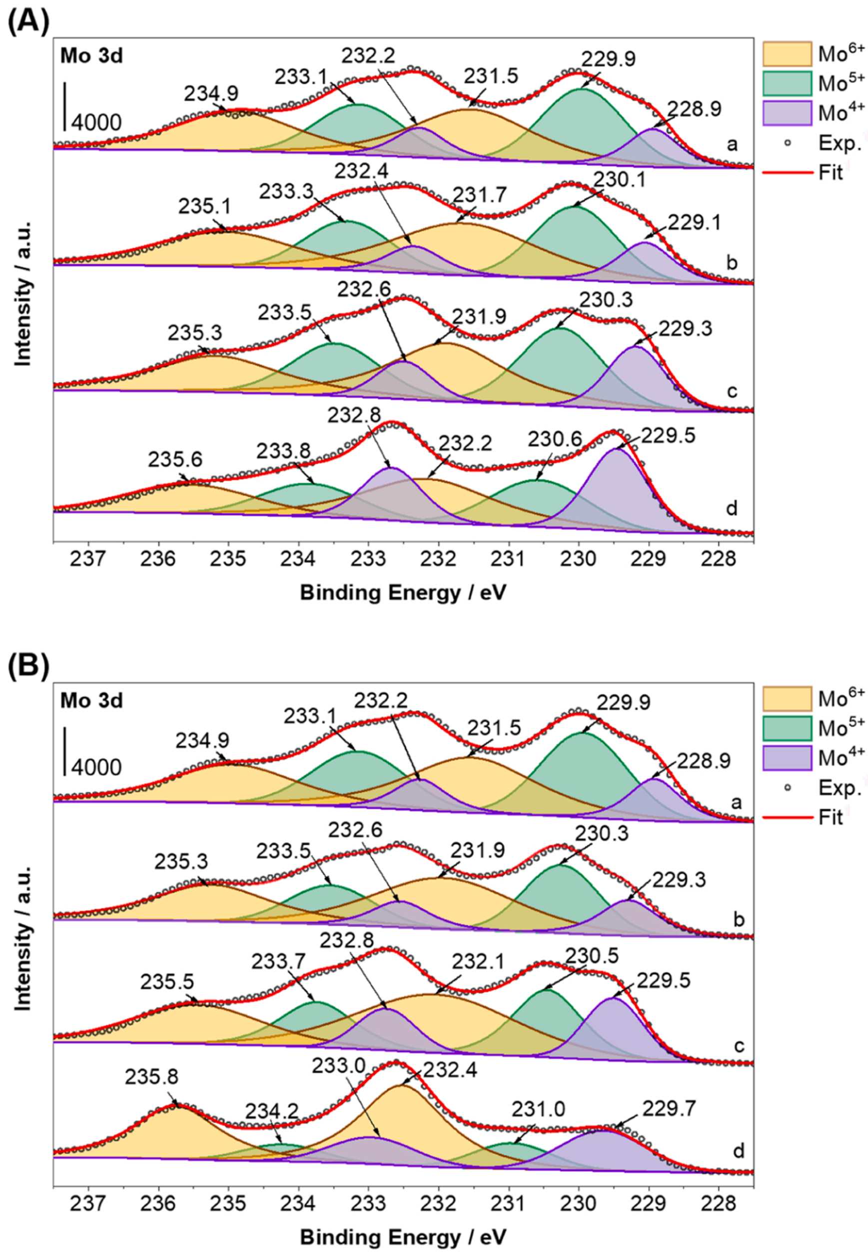

Fig. 7. Mo 3d XPS of the Co-Mo catalysts with different integration modes in the (A) initial states (2nd hour) and (B) steady states (20th hour). The $Pt_1/CoMoO_4$ (a) was the sample of the 30th hour. (a) $Pt_1/CoMoO_4$, (b) $CoMoO_4$, (c) 17Co-MoO_3, and (d) Co&Mo Mixed.

images, it is believed that the Co^0 and the Co-Mo interaction sites can be considered as the active sites for activating H_2, RAC, and HDO reactions. And the synergistic effects of Co^0 and LAS should be the essential part of selective hydrogenolysis sorbitol to EtOH. Additionally, with the introduction of the Pt_1 single atom promoter, the Co^0 and Co-Mo interaction sites exhibit more stable chemical states during the hydrogenolysis reaction over the $Pt_1/CoMoO_4$ catalyst.

3.2.2. *The chemical states of various catalysts*

The reduction behavior of various catalysts was characterized by H_2-TPR to describe the influence of different integration modes for the Co-Mo catalysts (Fig. 5). For the $CoMoO_4$ catalyst, the reduction peaks at 464 ℃ and 540 ℃ are corresponding to the reduction of $CoMoO_4$ and MoO_x species, respectively [35]. For the $Pt_1/CoMoO_4$ catalyst, both reduction peaks exhibit a downshift toward lower temperature, suggesting that the addition of Pt can effectively promote the reduction due to the hydrogen spillover effect via the added Pt [19,36]. On the other hand, for the Co&Mo Mixed catalysts, the broad peak at ~359 ℃ is attributed to the reduction of Co_3O_4 to CoO and then to metallic Co species [27,37]. And the higher reduction peak at 494 ℃ should assigned to the partial reduction of MoO_3 [38]. Moreover, the peak at ~447 ℃ can be assigned to the reduction of the in-situ generated $CoMoO_4$ located at the interface of the Co_3O_4 and MoO_3 [35,39]. Additionally, the reduction of Co_3O_4 over the 17Co-MoO_3 catalyst (~384 ℃) is higher than that of the Co&Mo Mixed catalyst, indicating that the stronger interaction between Co and Mo species over the 17Co-MoO_3 catalysts, as described as XRD and Raman results. Moreover, the shoulder peak at 480 ℃ can be known as the reduction peak of $CoMoO_4$ species which overlapped with the continuous reduction of CoO to Co [37]. Besides, the reduction peak with strong intensity at 549 ℃ is attributed to the MoO_3 reduction [27]. It can be found that the various CoMo heterostructure catalysts display totally different reducibility. It is considered that the different chemical environments caused by the different preparation methods and the added Pt_1 promoter would

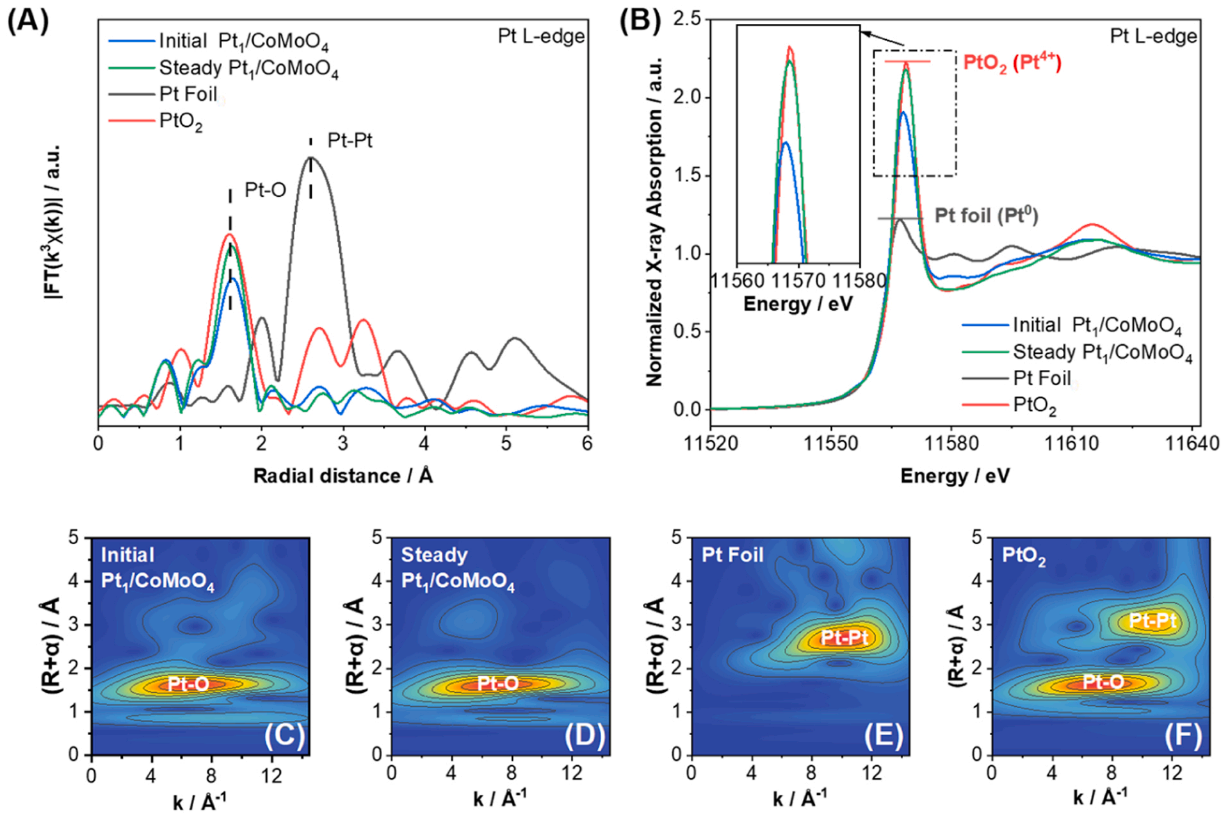

Fig. 8. (A)The normalized XANES and (B) EXAFS spectra in R-space of the $Pt_1/CoMoO_4$ in the (C) initial (2nd hour) and (D) steady (30th hour) states with references for Pt foil and PtO_2. The EXAFS wavelet transforms plots of the $Pt_1/CoMoO_4$ in the initial (C) and steady (D) states. And the EXAFS wavelet transforms plots of the Ref. Pt foil (E) and Ref. PtO_2 (F).

influence the acid sites and active sites of hydrogenation, which lead to different performance of sorbitol hydrogenolysis over the different catalysts.

To clarify the surface chemical state of CoMo catalysts, the XPS measurement was carried out. Before XPS characterization, the spent samples were preserved in N_2 atmosphere to avoid oxidation in the air.

The XPS results of Co 2p for the different initial catalysts are shown in Fig. 6 A and Table S3. For the $CoMoO_4$ catalysts, the peaks at 778.7 and 794.1 eV are attributed to Co $2p^{3/2}$ and Co $2p^{1/2}$ of Co^0 species, and peaks at 781.0 and 796.8 eV should be assigned to the CoO species [14]. Meanwhile, the peaks with higher binding energy at 782.4 and 798.2 eV are assigned to Co $2p^{3/2}$ and Co $2p^{1/2}$ of Co-O-Mo structure due to the electron transfer from Co to Mo, noted as $Co^{\delta+}$ [31,40]. And, the peaks at 787.0 and 803.5 eV can be known as the satellite peaks of Co species [41].

For the initial Co&Mo Mixed catalysts, the binding energy of $Co^{\delta+}$ species has a downshift to 781.8 eV, indicating that the decreased electron transfer from Co to Mo is due to the weak interaction between Co and Mo. But, the highest content of Co^0 (Table S3) was detected on the surface of the initial Co&Mo Mixed catalysts due to the weak interaction between Co and Mo species. As listed in Table S3, the initial $CoMoO_4$ catalyst has a higher content of $Co^{\delta+}$ species but the least content of Co^0, which is in line with the result of H_2-TPR. However, with the Pt_1 single atom promoter added, the content of Co^0 species increases dramatically and Co^{2+} species significantly decreases compared to $CoMoO_4$ catalyst as listed in Table S3. These results corroborate that the added Pt_1 promoter boosts the reduction of Co^{2+} species, resulting in an increased content of Co^0 than that of $CoMoO_4$ catalyst. It could be considered that a higher content of Co^0 species can promote the H_2 activation [42], which would facilitate the hydrogenolysis of sorbitol to EtOH [22]. Furthermore, the $Co^{\delta+}$ content of the initial $Pt_1/CoMoO_4$ is the highest in various catalysts, suggesting that more Co-Mo interaction sites formed as proved by Raman results. It is considered that Co-Mo interaction sites can be known as the LAS for facilitating the RAC reaction to cleave C-C bonds selectivity for generating C_2 intermediate [7] and the activating C-O in the HDO reaction to cleave C-O bonds assisted by the hydrogenation active sites [43], contributing to the higher EtOH selectivity.

Furthermore, the dynamic transformation of surface composition for Co species was also collected (Fig. 6 B and Table S3). Compared to the initial samples, the $CoMoO_4$, 17Co-MoO_3, and Co&Mo Mixed catalysts in the steady state show the sharply decreased content of Co^0 and $Co^{\delta+}$ species as listed in Table S3. However, the $Pt_1/CoMoO_4$ catalyst in steady state exhibits the highest content of Co^0 (10.5%) and $Co^{\delta+}$ (61.1%) due to the special promotional effects of the added Pt_1 promoter, contributing to the excellent stability during the reaction. Meanwhile, except for the $Pt_1/CoMoO_4$, the Co species of all samples in steady state shift towards lower banding energy as illustrated in Fig. 6 and Table S3, because the oxidation of Co^0 species weakens the interaction between Co and Mo species resulting in high electron density of Co species. Therefore, the added Pt_1 promoter not only keeps the stable interaction between Co and Mo but also maintains the content of Co^0 species, which results in high activity and EtOH selectivity with outstanding stability for sorbitol hydrogenolysis.

The XPS spectra of Mo 3d for the various catalysts in the initial and steady states are compared in Fig. 7 and Table S4. For the $CoMoO_4$ catalyst, the fitted peaks at 229.1 and 232.4 eV are assigned to Mo^{4+} $3d^{5/2}$ and $3d^{3/2}$, respectively [38]. And the peaks of Mo^{5+} $3d^{5/2}$ and $3d^{3/2}$ are located at 230.1 and 233.3 eV [44]. Meanwhile, the other spin-orbit doublet peaks at 231.7 and 235.1 eV are attributed to Mo^{6+} $3d^{5/2}$ and $3d^{3/2}$ [31,45]. As shown in Fig. 7A, the $CoMoO_4$ and $Pt_1/CoMoO_4$ in the initial state display lower binding energy of Mo species (especially Mo^{5+} and Mo^{6+} species) than the other samples in the initial state, indicating that more electrons transfer from Co to Mo

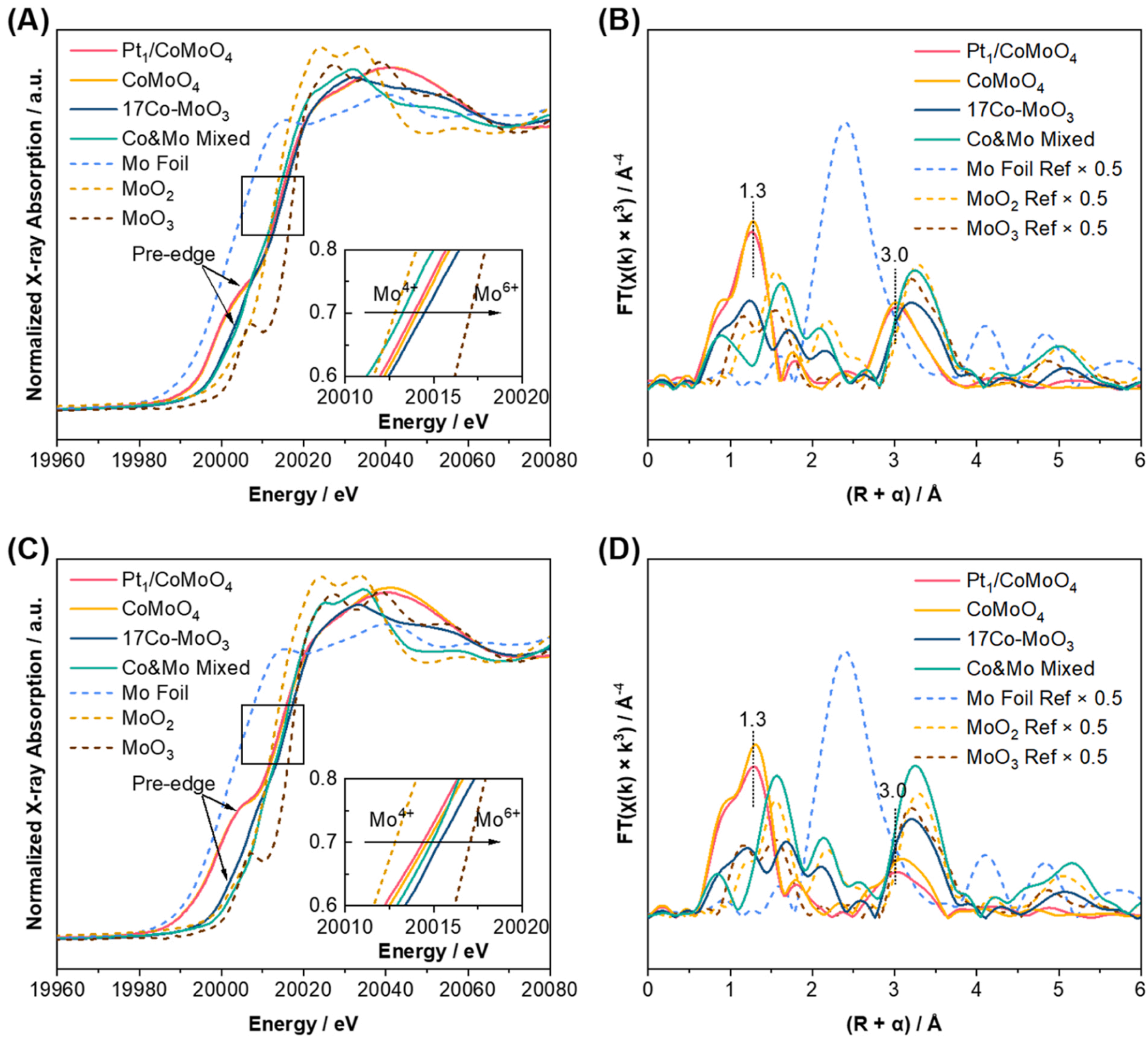

Fig. 9. The normalized Mo K-edge XANES spectra of the various CoMo heterostructure catalysts in the (A) initial states (2nd hour) and (C) steady (20th hour) with references for Mo foil, MoO_2, and MoO_3. (B) The non-phase corrected, k^3 weight Fourier-transformed EXASF spectra at Mo K-edge of the various CoMo heterostructure catalysts in the (A) initial states (2nd hour) and (C) steady (20th hour) with references for Mo foil, MoO_2, and MoO_3. The $Pt_1/CoMoO_4$ in steady state was the sample of the 30th hour.

resulting in higher electron density of Mo species on these catalysts due to stronger interaction between Co and Mo [31,40], as proved by Co 2p XPS. Besides, for the initial $Pt_1/CoMoO_4$, the lower binding energy of Mo species indicates the added Pt_1 promoter donates electrons to Mo species resulting in higher electron density [46]. Moreover, as listed in Table S4, the added Pt_1 promoter facilitates the formation of Mo^{5+}, leading to the highest content of Mo^{5+} among the various catalysts which was recognized as the active sites for C-O hydrogenolysis [12,38]. And the acid sites are widely known as the vital active site for cleaving C-C via RAC reaction to convert C_6 to C_2 intermediates in the sorbitol hydrogenolysis [7]. Thus, the highest content of Mo^{5+} can be known as one of the reasons for the highest EtOH selectivity.

Meanwhile, with the time on stream of the reaction, the chemical states of Mo species also exhibit dynamic transformation (Fig. 7B). For all catalysts except for $Pt_1/CoMoO_4$ in steady state, the binding energy of Mo species shifts to a higher value, indicating that the decreased electron density of Mo species corresponds to the decreased electron transform from Co to Mo [31,40]. However, the binding energy of Mo species on the $Pt_1/CoMoO_4$ catalyst in a steady state has no obvious changes, suggesting that the added Pt_1 promoter maintains the surface electronic properties of the $Pt_1/CoMoO_4$ catalyst contributing to excellent stability. Besides, as described in Table S4, the $Pt_1/CoMoO_4$ catalyst in the steady state retains the highest content of Mo^{5+}, demonstrating that the added Pt_1 promoter contributes to maintaining the Mo^{5+} species, which would benefit for steadily selective hydrogenolysis sorbitol to EtOH.

To reveal the nature of the single-Pt-atom on the $Pt_1/CoMoO_4$ catalyst in the initial and steady states, XANES and EXAFS spectrometry were performed. As shown in Fig. 8 A, the Pt-Pt contribution at 2.7 Å is absent in the k^3-weighted EXAFS at the Pt L-edge for either $Pt_1/CoMoO_4$ in the initial or steady states, but only the salient peak located at 1.7 Å which arisen from Pt-O contribution [47], suggesting that Pt species exist as the isolated atoms [20,48]. Moreover, the WT-EXAFS of the $Pt_1/CoMoO_4$ in the initial and steady states also proved the formation of Pt single atoms on the $Pt_1/CoMoO_4$ catalyst [47], as illustrated in Fig. 8 (C-F). Therefore, it is believed that the Pt_1 promoter is advantageous to activating H_2 for generating Co^0 and Mo^{5+} sites and preventing them from oxidation during the hydrogenolysis reaction [49], as proved by Raman and XPS results.

Furthermore, the fitting results of EXAFS curves are summarized in

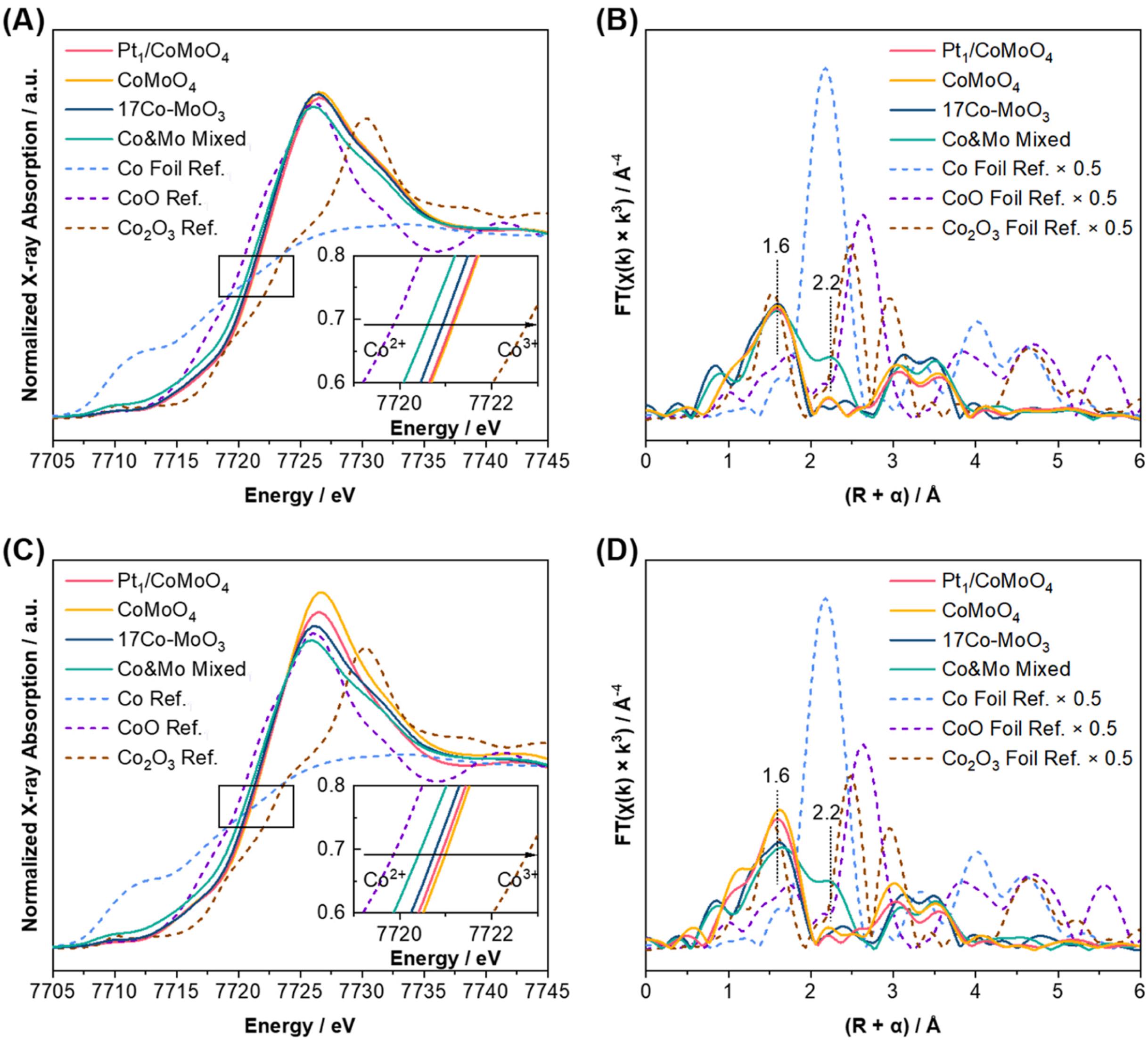

Fig. 10. The normalized Co K-edge XANES spectra of the various CoMo heterostructure catalysts in the (A) initial states (2nd hour) and (C) steady (20th hour) with references for Co foil, CoO, and Co_2O_3. (B) The non-phase corrected, k^3 weight Fourier-transformed EXAFS spectra at Co K-edge of the various CoMo heterostructure catalysts in the (A) initial states (2nd hour) and (C) steady (20th hour) with references for Co foil, CoO, and Co_2O_3. The $Pt_1/CoMoO_4$ in steady state was the sample of the 30th hour.

Fig. S5-S6 and Table S5. Compared with the initial sample, the steady $Pt_1/CoMoO_4$ sample exhibits a stronger intensity of Pt-O coordination. And the fitted Pt-O coordination number increased from 5.3 to 6.2, demonstrating the slight transformation of the Pt chemical state with the time on stream [50,51]. Furthermore, the electronic states of Pt species were investigated by XANES (Fig. 8 B). It can be apparently discerned that the overall white line intensity in the steady state is much higher than that in the initial state, indicating that Pt donates more electrons with the time on stream of the reaction [50,52]. Combined with the results of XPS, it is believed that the electron transfer from Pt to $CoMoO_4$ is the reason for maintaining the chemical states of the Co^0 and Mo^{5+} sites [17,46].

Fig. 9 shows the normalized Mo K-edge XANES spectra of various catalysts. The pre-edge of $CoMoO_4$ and $Pt_1/CoMoO_4$ can be known as the feature of molybdate species caused by the interaction between Co and Mo species in Fig. 9A [53], and they are obviously stronger than that of the 17Co-MoO_3 and Co&Mo Mixed due to more Co-Mo interaction sites, as proved by Raman. Moreover, the state of Mo species can be further analyzed by the Mo K-edge of the various catalysts in the inset of Fig. 9 (A and C). The Mo K-edge energy of all samples is located between MoO_2 and MoO_3, indicating the oxidation state of Mo is between +4 and +6 [54]. Shetty et al. reported that the partially reduced Mo species can be known as LAS [55], which would be the active site of the RAC and HDO reaction for sorbitol hydrogenolysis [12,38]. Additionally, as shown in Fig. 9 C, the Mo K-edge of $CoMoO_4$, 17Co-MoO_3, and Co&Mo Mixed catalysts shift to higher energy, indicating that the oxidation of Mo species during reaction decreased Mo electron density [56]. However, the $Pt_1/CoMoO_4$ catalyst only exhibits a very slight shift in Mo K-edge, suggesting the added Pt_1 significantly promotes the stability of Mo species.

Additionally, FT-EXAFS spectra and the fitting results of the various catalysts in initial and steady states are shown in Fig. 9 (B and D), Fig. S7-S8, and Table S6-S7. As shown in Fig. 9, The peak around ~1.3 Å is assigned to the Mo-O scattering feature [57], and the peak at around ~3.0 Å is attributed to the Mo-O-Co scattering for $CoMoO_4$ and $Pt_1/CoMoO_4$ [58,59]. As compared in Table S6 and S7, the Mo-O-Co scattering of the $CoMoO_4$ and $Pt_1/CoMoO_4$ has a lower R value than that of 17Co-MoO_3 and Co&Mo Mixed catalysts, manifesting stronger interaction between Mo and Co on $CoMoO_4$ and $Pt_1/CoMoO_4$ catalysts [60], as proved by Raman results. Meanwhile, the strong interaction

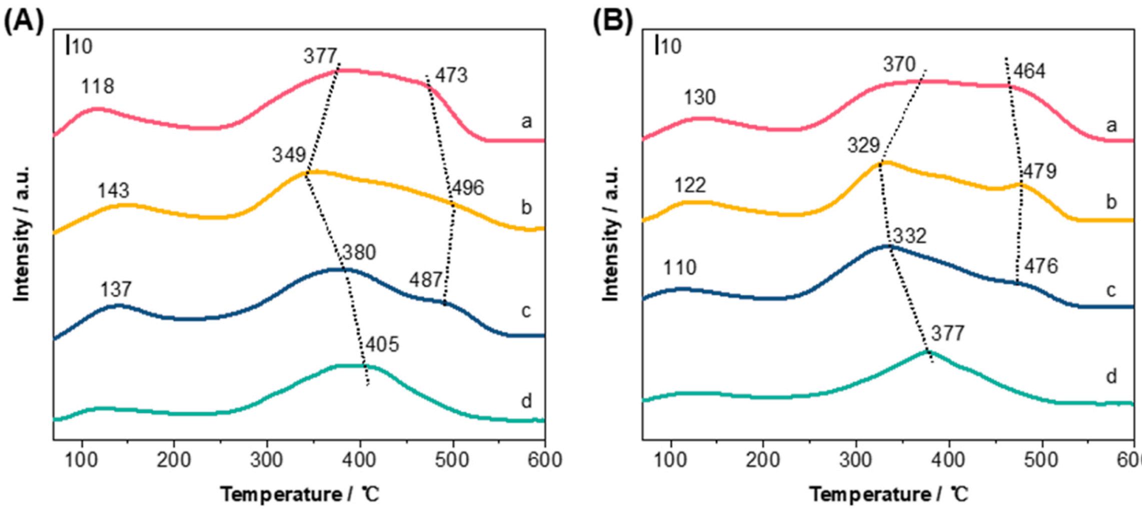

Fig. 11. NH_3-TPD of various catalysts in the (A) initial (2nd hour) and (B) steady (20th hour) states. The $Pt_1/CoMoO_4$ (a) was the sample of the 30th hour. (a) $Pt_1/CoMoO_4$, (b) $CoMoO_4$, (c) 17Co-MoO_3, (d) Co&Mo Mixed.

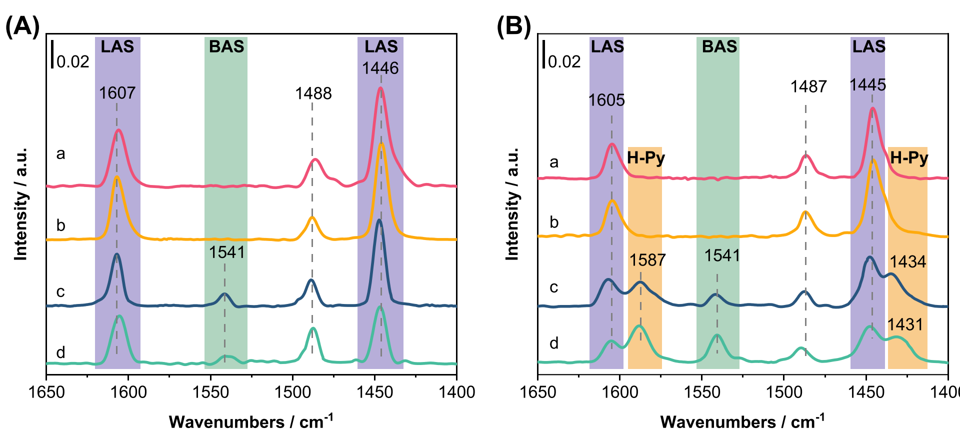

Fig. 12. Py-FTIR of various CoMo heterostructure catalysts in the (A) initial (2nd hour) and (B) steady (20th hour) states. The $Pt_1/CoMoO_4$ (a) was the sample of the 30th hour. (a) $Pt_1/CoMoO_4$, (b) $CoMoO_4$, (c) 17Co-MoO_3, and (d) Co&Mo Mixed.

between Co and Mo on the catalysts is advantageous to forming more Lewis acid sites, which would contribute to cleaving C-C bonds for hydrogenolysis sorbitol to form more C_2 (EG + EtOH) products [7,28].

The Co K-edge XANES and FT-EXAFS spectra are shown in Fig. 10. For the $CoMoO_4$ and $Pt_1/CoMoO_4$, the Co K-edge exhibits higher Co K-edge energy than that of the 17Co-MoO_3 and Co&Mo Mixed catalysts as illustrated in Fig. 10A inset, suggesting the lower Co electron density is obtained [61]. It can be known as the result of the electron transfer from Co to Mo, which is consistent with the XPS and Mo K-edge results. And the K-edge of the $Pt_1/CoMoO_4$ slightly shifts to lower energy compared to $CoMoO_4$ due to the added Pt_1 promoter facilitating the reduction of Co. Interestingly, for the samples in steady state, the Co K-edge of 17Co-MoO_3 and Co&Mo Mixed catalyst shift to lower energy as shown in the inset of Fig. 10C indicating higher Co electron density induced by the weakened interaction between Co and Mo. Additionally, compared to the initial sample, higher intensity of the white line for the $CoMoO_4$ and $Pt_1/CoMoO_4$ in the steady state indicates that the oxidation of the partially reduced $CoMoO_4$ species [62], which would lead to the decreased acidity of LAS sites [55]. Comparatively, the $Pt_1/CoMoO_4$ catalyst is more stable. It can be believed that the added Pt_1 promoter inhibits the oxidation of the partially reduced $CoMoO_4$ species and maintains the LAS acidity and activity of sorbitol hydrogenolysis [12,38].

Meanwhile, Fig. 10 B and D show the Co K-edge FT k^3-weight EXAFS spectra of the initial and steady catalysts. And the curve fitting results of EXAFS data are summarized in Fig S10-S11 and Table S8-S9. As shown in Fig. 10B, for the initial catalysts, the peaks centered at ~1.6 Å are corresponding to the single-scattering path of Co-O [63]. As listed in Tables S8 and S9, the CN of Co-O paths increases with time on stream of the reaction for all steady samples. However, the $Pt_1/CoMoO_4$ shows the least difference, indicating that higher stability is obtained due to the Pt_1 promoter added. Meanwhile, the $Pt_1/CoMoO_4$ exhibits the lowest degree of decline of the Co-(O)-Mo coordination number, proving that the more interaction sites between Co and Mo are preserved on the $Pt_1/CoMoO_4$ catalyst, which can be known as the reason for higher efficiency and stability on sorbitol hydrogenolysis.

3.2.3. Acid properties of different catalysts

As shown in Fig. 11A and B, the surface acidic properties of various catalysts in the initial and steady states were studied via ammonia temperature-programmed desorption (NH_3-TPD). In order to avoid oxidation by air, the spent samples were all preserved in N_2 before NH_3-TPD characterization. All catalysts realize a wide range of desorption as shown in Fig. 11, demonstrating various acid sites are generated for effectively converting sorbitol to EtOH.

As shown in Fig. 11A, the desorption peaks below 300 ℃ are known as weak acid sites, and the peaks at 300–450 ℃ and above 450 ℃ correspond to medium and strong acid sites, respectively [64]. It is

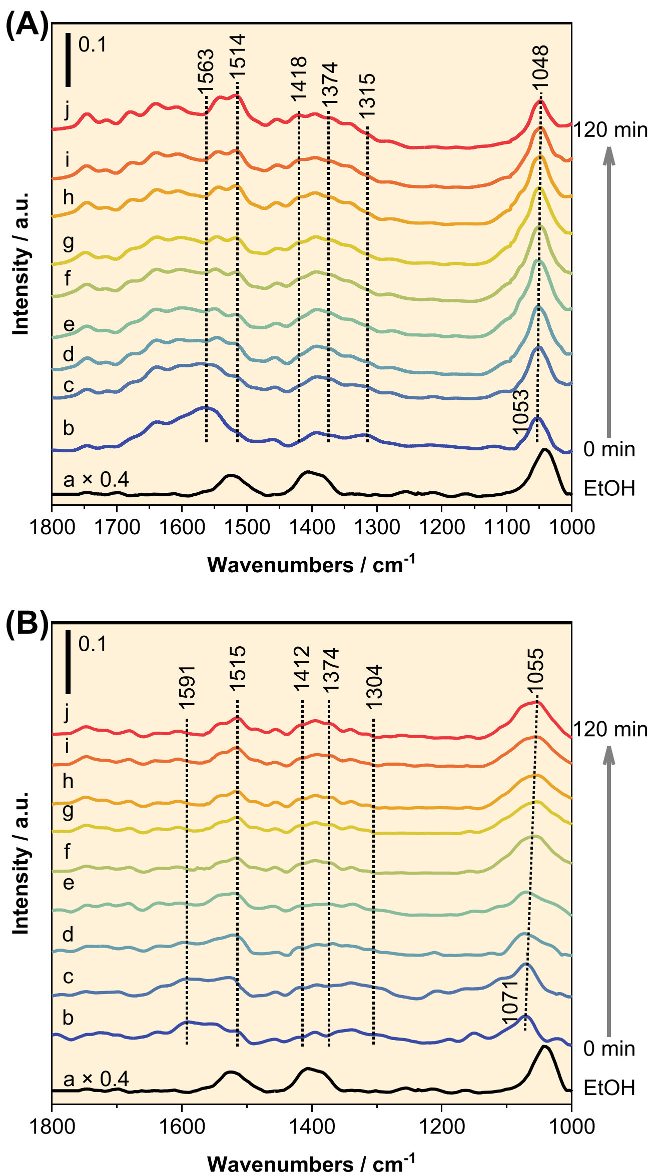

Fig. 13. Operando EG-DRIFTS over the (A) $Pt_1/CoMoO_4$ and (B) Co&Mo Mixed. Line (a) in both figures refers to EtOH adsorption on the $Pt_1/CoMoO_4$. Line (b) refers to EG adsorption on the $Pt_1/CoMoO_4$ and Co&Mo Mixed catalysts, respectively. Line (c-j) collected every 15 min after H_2 introduction.

worth stating that a broad desorption peak of the medium acid sites on the $Pt_1/CoMoO_4$ catalyst located at a relatively high temperature (377 ℃), caused by the moderate interaction between Co and Mo which can avoid forming low active sites by too strong or weak acidity [65,66]. Furthermore, the medium acid site is always recognized as the active site for catalyzing the RAC reaction to convert sorbitol to C_2 intermediates [7]. For the $Pt_1/CoMoO_4$, the added Pt_1 promoter adjusts the interaction between Co and Mo to generate more Mo^{5+} species and the more appropriate medium acid sites for facilitating hydrogenolysis sorbitol to EtOH.

Compared to the initial samples, the desorption peaks of the steady catalysts exhibit a negative shift to lower temperature as shown in Fig. 11 B, which is due to the decline of the CN of Co-O-Mo and the content of Mo^{5+} as proved by EXAFS and XPS results. However, for the $Pt_1/CoMoO_4$ catalysts, the less decrease of the medium acid sits is realized due to the stable chemical states of Co and Mo species. It is believed that the added Pt_1 single atom promoter is advantageous to steadily and efficiently convert sorbitol to EtOH.

The Pyridine-Fourier Transform Infrared spectroscopy (Py-FTIR) was employed to detect the properties of Lewis and Brønsted acid on the various catalysts, and the results are shown in Fig. 12. For the initial catalysts (Fig. 12A). Vibrational modes observed at 1446 and 1607 cm^{-1} should be corresponded to pyridine coordinated to LASs, and the band at 1488 cm^{-1} is attributed to the combination of LASs and BASs [67,68]. Meanwhile, the band at ~1541 cm^{-1} should be assigned to pyridine protonated to BASs [69,70]. Furthermore, to reveal the dynamic transformation of surface acid properties, the Py-FTIR of the steady catalysts was also carried out as shown in Fig. 12B. It was reported that the cooperation between LAS and BAS could promote the isomerization of glucose to fructose, resulting in high selectivity of C_3 products [71,72]. In Fig. 12B, the new bands at 1587 and ~1434 cm^{-1}, which are assigned to the hydrogen (H)-bonded pyridine at hydroxy sites [73], can be observed on the steady 17Co-MoO_3 and Co&Mo Mixed catalysts due to the decreased Mo electron density during the reaction as proved by XPS and XANES [57]. Additionally, this hydrogen bonded hydroxy is advantageous to generating BAS during the reaction, leading to the higher content of BAS on the catalysts surface, as shown in Fig. 12B [57]. Therefore, the formation of BASs during reaction leads to lower EtOH selectivity over the 17Co-MoO_3 and Co&Mo Mixed catalysts. On the other hand, the LAS band of the $CoMoO_4$ becomes wider than that of $Pt_1/CoMoO_4$ catalysts, suggesting more changes in acid properties on the surface of the $CoMoO_4$ catalyst. On the other hand, as compared in Table S10, the acid amount of various catalysts indicates that the $Pt_1/CoMoO_4$ catalyst realized the highest acid amount due to the promotional effects of Pt_1 on forming and keeping acid sites, contributing to the best reaction performance in this study.

As previously reported [3,22], converting EG to EtOH can be recognized the one of the essential steps of selective hydrogenolysis sorbitol to EtOH. Therefore, the catalytic performance of EG to EtOH via the $Pt_1/CoMoO_4$ and Co&Mo Mixed catalysts was monitored by operando EG-DRIFTS measurements (Fig. 13). The EG was introduced into the in-situ reaction cell by N_2 at 245 ℃ for 1 h. And the physically adsorbed EG was swept by N_2 flow for 1 h, subsequently. After that, H_2 was introduced into the cell and the spectra were collected every 15 min.

As shown in Fig. 13A Line b, a broad band centered at 1563 cm^{-1} could be observed after EG adsorbing on the $Pt_1/CoMoO_4$ catalyst. The band at 1563 cm^{-1} can be attributed to the υ(OCO) of the adsorbed glycolate, and the band at 1315 cm^{-1} also corresponds to the adsorbed glycolate [74–76]. Additionally, in Fig. 13B Line b, a broad band at 1591 cm^{-1} with a shoulder peak at 1563 cm^{-1} can be found for the Co&Mo Mixed catalyst where the band at 1591 cm^{-1} should be attributed to the υ(C=O) of the adsorbed glycolaldehyde [74]. Moreover, the bands at 1053 cm^{-1} and 1071 cm^{-1} are corresponding to the υ(C-O) of the adsorbed glycolate or glycolaldehyde [74–76]. Comparing the intensity of the adsorbed EG spectra for different catalysts, it is suggested that more active sites for adsorbing EG were generated on the surface of the $Pt_1/CoMoO_4$ catalyst figuring out the higher EG activating ability.

After the introduction of hydrogen from Fig. 13 A line c, the band intensity of the adsorbed glycolate drastically decreases with the rapidly increasing intensity of the band at ~1053 cm^{-1}, implying the hydrogenation of the adsorbed glycolate. Meanwhile, according to Line a (references of the adsorbed EtOH), the increasing intensity of the band at ~1514 cm^{-1} or 1515 cm^{-1} also proves the formation of EtOH after H_2 introduction. Simultaneously, the band intensity of $\delta_s(CH_3)$ and $\delta_{as}(CH_3)$, located at 1418 and 1374 cm^{-1}, significantly increases with time on stream, suggesting the formation of the -CH_3 group of EtOH with the H_2 introduction [77,78]. Furthermore, the band of the -CH_3 group is formed in 15 min after H_2 introduction (Fig. 13A, Line c) for the $Pt_1/CoMoO_4$. However, the obvious strengthening of the -CH_3 band over the Co&Mo Mixed can be observed after the longer interaction between EG and H_2 (Fig. 13B, Line f), suggesting that the $Pt_1/CoMoO_4$ exhibits higher hydrogen activity, leading to the much higher efficiency for EG hydrogenolysis.

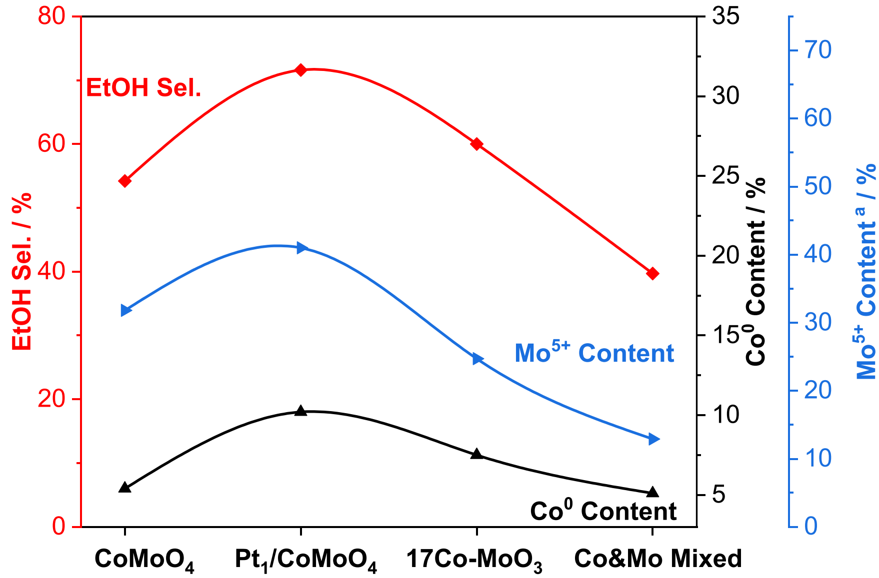

Fig. 14. EtOH selectivity and Co^0 and Mo^{5+} content (based on XPS results of the steady samples) as a function of the various CoMo heterostructure catalysts.

Additionally, the EG hydrogenolysis over the $Pt_1/CoMoO_4$ and Co&Mo Mixed catalysts was tested using a continuous-flow fixed bed reactor. Similar to the literature [3], the products of EG hydrogenolysis were mainly EtOH and ethane, as shown in Table S11, and the $Pt_1/CoMoO_4$ catalyst realized higher EG conversion and EtOH selectivity than the Co&Mo Mixed catalyst. It is further proved that the $Pt_1/CoMoO_4$ catalyst is advantageous to hydrogenolysis of EG to EtOH as confirmed by operando EG-DRIFTS, contributing to the highest EtOH selectivity during sorbitol hydrogenolysis.

Consequently, for the $Pt_1/CoMoO_4$, the added Pt single atom promoter generates more Mo^{5+} sites (contributing to the formation of appropriate medium acid sites and LASs) and Co^0 hydrogenation active sites, leading to the facilitated C_2 intermediate formation and conversion, resulting in the highest EtOH selectivity. Therefore, it is rational to consider that the Pt_1 single atom addition effectively adjusts the synergistic effects between the Mo^{5+} and Co^0 active sites to improve the formation of EtOH.

As illustrated in Fig. 14, the EtOH selectivity of the various catalysts is correlated with the content of Co^0 and Mo^{5+} species. On one hand, in terms of Mo^{5+} species, the $CoMoO_4$ catalyst has more Mo^{5+} sites and similar Co^0 content to the Co&Mo Mixed catalysts, indicating that the generated Mo^{5+} sites play an important role in sorbitol hydrogenolysis to EtOH. Furthermore, the interaction and electron transfer between Co and Mo on $Pt_1/CoMoO_4$, as confirmed by Raman, XPS, and XANES, contributes to the formation of the most Mo^{5+} sites. As confirmed by NH_3-TPD and Py-FTIR, the highest content of Mo^{5+}, depicted in Fig. 14, makes the $Pt_1/CoMoO_4$ generate the higher content of LASs with medium acidity, which promotes the sorbitol converting to EG intermediate with C-C bond cleaving via RAC reaction [7,66]. On the other hand, the content of the Co^0 species is in an order of $Pt_1/CoMoO_4 > 17Co\text{-}MoO_3 > CoMoO_4 >$ Co&Mo Mixed, based on the Co XPS result. Co^0 can serve as a hydrogenation active site which has a positive effect on converting EG intermediate to EtOH via hydrogenation in sorbitol hydrogenolysis reaction [3,22]. For the Co&Mo Mixed catalyst, the Co^0 species could be rapidly oxidized during the reaction proceeds, as proved by Co XPS in Fig. 6. The lower content of Co^0 on the Co&Mo Mixed in the steady state could be the reason for the inferior performance compared with the one in the initial state.

It is challenge to improve the target product selectivity of the sorbitol hydrogenolysis process as multiple reaction steps and side reactions are involved in the conversion of sorbitol to ethanol. In previous studies, it was reported that sorbitol could be converted to glucose intermediate at first [5,6]. Then, glucose can be converted to C2 and C4 intermediates by selectively cleaving C-C bonds via RAC reaction promoted by LAS [7, 28]. In addition, the C4 intermediate can also be converted to C2 intermediates in the same way. On one hand, in this reaction step, too strong or weak acidity of the catalyst would suppress the RAC reaction [65,66]. Importantly, more Mo^{5+} LAS sites with appropriate acid strength were generated on the $Pt_1/CoMoO_4$ catalysts, which contributes the higher selectivity of the C2 product. On the other hand, the BAS can promote isomerization of glucose to forming fructose which is the key intermediate of generating C3 products [71,72]. Therefore, no BAS on $Pt_1/CoMoO_4$ catalyst inhibits the side reaction for forming C3 products, contributing to high C2 product selectivity. Meanwhile, the active sites of hydrogenation play an important role in promoting the HDO reaction in the conversion of the C2 intermediate from RAC reaction to EtOH [29]. As proved above, the added Pt promoter effectively contributes to generation of Co^0 and maintaining its chemical state on the $Pt_1/CoMoO_4$ catalyst, which leads to the highest EtOH selectivity.

Therefore, benefitting from the highest content of Mo^{5+} and Co^0 on the $Pt_1/CoMoO_4$, the RAC of sorbitol and hydrogenation of EG intermediate can be facilitated simultaneously. It is conducive to efficiently converting sorbitol to EtOH. Besides, the Pt_1 promoter not only improves the generation of Co^0 and Mo^{5+} to build the efficient synergistic effect between LAS and the hydrogenation site but also maintains the chemical state of Mo^{5+} and Co^0 during the hydrogenolysis reaction. Therefore, the $Pt_1/CoMoO_4$ catalyst displays the best catalytic performance with 99.6% sorbitol conversion and 71.6% EtOH selectivity, and the $Pt_1/CoMoO_4$ catalyst also shows much better stability than the other CoMo heterostructure catalysts.

4. Conclusion

The various CoMo heterostructure catalysts were employed in the selective hydrogenolysis of sorbitol to EtOH via a continuous-flow fixed-bed reactor. Combined with the series of characterizations, it is found that the synergistic effects between Co^0 and the Mo^{5+} sites, which contribute to the formation of hydrogenation active sites and LASs with medium acidity. It is essential for converting sorbitol to EtOH. Besides, the Pt_1 single atom promoter contributes to tuning electron transfer between Co and Mo to establish more stable catalytic properties with the highest content of Co^0 and Mo^{5+} sites, which effectively promotes the stable formation of ethanol from sorbitol hydrogenolysis.

CRediT authorship contribution statement

Yi Zhang: Writing – review & editing, Supervision, Project administration, Funding acquisition, Conceptualization. **Honglin Zhuang:** Data curation. **Ling Zhou:** Supervision, Conceptualization. **Jiacheng Ji:** Writing – original draft, Investigation, Data curation.

Declaration of Competing Interest

The authors declare that they have no known competing financial interests or personal relationships that could have appeared to influence the work reported in this paper.

Data availability

Data will be made available on request.

Acknowledgment

This work is supported by Bingtuan Science and Technology Program (2021DB006), National Natural Science Foundation of P. R. China (U20B2022 and 22078006).

Appendix A. Supporting information

Supplementary data associated with this article can be found in the online version at doi:10.1016/j.apcatb.2024.123890.

References

[1] B. Liu, Y. Nakagawa, C. Li, M. Yabushita, K. Tomishige, Selective C–O hydrogenolysis of terminal C–OH bond in 1,2-diols over rutile-titania-supported iridium-iron catalysts, ACS Catal. 12 (2022) 15431–15450, https://doi.org/10.1021/acscatal.2c04499.

[2] R.F. Service, Is there a road ahead for cellulosic ethanol, Science 329 (2010) 784–785, https://doi.org/10.1126/science.329.5993.784.

[3] M. Yang, H. Qi, F. Liu, Y. Ren, X. Pan, L. Zhang, X. Liu, H. Wang, J. Pang, M. Zheng, A. Wang, T. Zhang, One-pot production of cellulosic ethanol via tandem catalysis over a multifunctional Mo/Pt/WO_x catalyst, Joule 3 (2019) 1937–1948, https://doi.org/10.1016/j.joule.2019.05.020.

[4] J.J. Bozell, G.R. Petersen, Technology development for the production of biobased products from biorefinery carbohydrates—the US Department of Energy's "Top 10" revisited, Green. Chem. 12 (2010) 539, https://doi.org/10.1039/b922014c.

[5] N.M. Eagan, J.P. Chada, A.M. Wittrig, J.S. Buchanan, J.A. Dumesic, G.W. Huber, Hydrodeoxygenation of sorbitol to monofunctional fuel precursors over Co/TiO_2, Joule 1 (2017) 178–199, https://doi.org/10.1016/j.joule.2017.07.004.

[6] I. Murillo Leo, M. López Granados, J.L.G. Fierro, R. Mariscal, Selective conversion of sorbitol to glycols and stability of nickel–ruthenium supported on calcium hydroxide catalysts, Appl. Catal. B Environ. 185 (2016) 141–149, https://doi.org/10.1016/j.apcatb.2015.12.005.

[7] Y. Liu, Y. Liu, Y. Zhang, The synergistic effects of Ru and WO_x for aqueous-phase hydrogenation of glucose to lower diols, Appl. Catal. B Environ. 242 (2019) 100–108, https://doi.org/10.1016/j.apcatb.2018.09.085.

[8] Y. Liu, Y. Liu, Q. Wu, Y. Zhang, Catalytic conversion of glucose into lower diols over highly dispersed SiO_2-supported Ru-W, Catal. Commun. 129 (2019) 105731, https://doi.org/10.1016/j.catcom.2019.105731.

[9] J. Ji, Y. Xu, Y. Liu, Y. Zhang, A nanosheet Ru/WO_3 catalyst for efficient conversion of glucose to butanediol, Catal. Commun. 144 (2020) 106074, https://doi.org/10.1016/j.catcom.2020.106074.

[10] K. Murugappan, E.M. Anderson, D. Teschner, T.E. Jones, K. Skorupska, Y. Román-Leshkov, Operando NAP-XPS unveils differences in MoO_3 and Mo_2C during hydrodeoxygenation, Nat. Catal. 1 (2018) 960–967, https://doi.org/10.1038/s41929-018-0171-9.

[11] P. Sudarsanam, N.K. Gupta, B. Mallesham, N. Singh, P.N. Kalbande, B.M. Reddy, B. F. Sels, Supported MoO_x and WO_x solid acids for biomass valorization: interplay of coordination chemistry, acidity, and catalysis, ACS Catal. 11 (2021) 13603–13648, https://doi.org/10.1021/acscatal.1c03326.

[12] L. Xiang, M. Liu, G. Fan, L. Yang, F. Li, MoO_x-decorated ZrO_2 nanostructures supporting Ru nanoclusters for selective hydrodeoxygenation of anisole to benzene, ACS Appl. Nano Mater. 4 (2021) 12588–12599, https://doi.org/10.1021/acsanm.1c03110.

[13] S. Zhang, J. Gan, Z. Xia, X. Chen, Y. Zou, X. Duan, Y. Qu, Dual-active-sites design of Co@C catalysts for ultrahigh selective hydrogenation of N-heteroarenes, Chem 6 (2020) 2994–3006, https://doi.org/10.1016/j.chempr.2020.07.023.

[14] K. An, S. Zhang, H. Wang, N. Li, Z. Zhang, Y. Liu, Co^0—$Co^{\delta+}$ active pairs tailored by Ga-Al-O spinel for CO_2-to-ethanol synthesis, Chem. Eng. J. 433 (2022) 134606, https://doi.org/10.1016/j.cej.2022.134606.

[15] R. Ding, Y. Wu, Y. Chen, H. Chen, J. Wang, Y. Shi, M. Yang, Catalytic hydrodeoxygenation of palmitic acid over a bifunctional Co-doped MoO_2/CNTs catalyst: an insight into the promoting effect of cobalt, Catal. Sci. Technol. 6 (2016) 2065–2076, https://doi.org/10.1039/C5CY01575H.

[16] J. Shan, M. Li, L.F. Allard, S. Lee, M. Flytzani-Stephanopoulos, Mild oxidation of methane to methanol or acetic acid on supported isolated rhodium catalysts, Nature 551 (2017) 605–608, https://doi.org/10.1038/nature24640.

[17] S. Fang, X. Zhu, X. Liu, J. Gu, W. Liu, D. Wang, W. Zhang, Y. Lin, J. Lu, S. Wei, Y. Li, T. Yao, Uncovering near-free platinum single-atom dynamics during electrochemical hydrogen evolution reaction, Nat. Commun. 11 (2020) 1029, https://doi.org/10.1038/s41467-020-14848-2.

[18] J. Jones, H. Xiong, A.T. DeLaRiva, E.J. Peterson, H. Pham, S.R. Challa, G. Qi, S. Oh, M.H. Wiebenga, X.I. Pereira Hernández, Y. Wang, A.K. Datye, Thermally stable single-atom platinum-on-ceria catalysts via atom trapping, Science 353 (2016) 150–154, https://doi.org/10.1126/science.aaf8800.

[19] J. Park, S. Lee, H. Kim, A. Cho, S. Kim, Y. Ye, J.W. Han, H. Lee, J.H. Jang, J. Lee, Investigation of the support effect in atomically dispersed Pt on WO_{3-x} for utilization of Pt in the hydrogen evolution reaction, Angew. Chem. Int. Ed. 58 (2019) 16038–16042, https://doi.org/10.1002/anie.201908122.

[20] J. Li, Q. Guan, H. Wu, W. Liu, Y. Lin, Z. Sun, X. Ye, X. Zheng, H. Pan, J. Zhu, S. Chen, W. Zhang, S. Wei, J. Lu, Highly active and stable metal single-atom catalysts achieved by strong electronic metal–support interactions, J. Am. Chem. Soc. 141 (2019) 14515–14519, https://doi.org/10.1021/jacs.9b06482.

[21] B. Ravel, M. Newville, *ATHENA*, *ARTEMIS*, *HEPHAESTUS*: data analysis for X-ray absorption spectroscopy using *IFEFFIT*, J. Synchrotron Rad. 12 (2005) 537–541, https://doi.org/10.1107/S0909049505012719.

[22] Y. Wu, C. Dong, H. Wang, J. Peng, Y. Li, C. Samart, M. Ding, One-pot ethanol production from cellulose transformation over multifunctional Pt/WO_x and hollow Pt@HZSM-5 catalysts, ACS Sustain. Chem. Eng. 10 (2022) 2802–2810, https://doi.org/10.1021/acssuschemeng.1c08204.

[23] J. Zhang, C. Li, W. Guan, X. Chen, X. Chen, C.-W. Tsang, C. Liang, Deactivation and regeneration study of a Co-promoted MoO_3 catalyst in hydrogenolysis of dibenzofuran, Ind. Eng. Chem. Res. 59 (2020) 4313–4321, https://doi.org/10.1021/acs.iecr.9b06442.

[24] F. Lu, X. Chen, Z. Lei, L. Wen, Y. Zhang, Revealing the activity of different iron carbides for Fischer-Tropsch synthesis, Appl. Catal. B Environ. 281 (2021) 119521, https://doi.org/10.1016/j.apcatb.2020.119521.

[25] Y. Ou, W. Tian, L. Liu, Y. Zhang, P. Xiao, Bimetallic $Co_2Mo_3O_8$ suboxides coupled with conductive cobalt nanowires for efficient and durable hydrogen evolution in alkaline electrolyte, J. Mater. Chem. A. 6 (2018) 5217–5228, https://doi.org/10.1039/C7TA11401J.

[26] J. Meng, J. Yang, J. Fang, N. Li, Y. He, H. Huang, J. Lu, Production of liquid fuels from low-temperature coal tar via hydrogenation over CoMo/USY catalysts, Reac Kinet. Mech. Cat. 127 (2019) 961–978, https://doi.org/10.1007/s11144-019-01576-y.

[27] J. Zhang, C. Li, W. Guan, X. Chen, X. Chen, C.-W. Tsang, C. Liang, Promotional effect of Co and Ni on MoO_3 catalysts for hydrogenolysis of dibenzofuran to biphenyl under atmospheric hydrogen pressure, J. Catal. 383 (2020) 311–321, https://doi.org/10.1016/j.jcat.2020.01.035.

[28] A. Wang, T. Zhang, One-pot conversion of cellulose to ethylene glycol with multifunctional tungsten-based catalysts, Acc. Chem. Res. 46 (2013) 1377–1386, https://doi.org/10.1021/ar3002156.

[29] X. Liu, W. Jia, G. Xu, Y. Zhang, Y. Fu, Selective hydrodeoxygenation of lignin-derived phenols to cyclohexanols over Co-based catalysts, ACS Sustain. Chem. Eng. 5 (2017) 8594–8601, https://doi.org/10.1021/acssuschemeng.7b01047.

[30] X. Zhang, L. Zhong, Q. Guo, H. Fan, H. Zheng, K. Xie, Influence of the calcination on the activity and stability of the Cu/ZnO/Al_2O_3 catalyst in liquid phase methanol synthesis, Fuel 89 (2010) 1348–1352, https://doi.org/10.1016/j.fuel.2009.06.011.

[31] R. Yao, J. Pinals, R. Dorakhan, J.E. Herrera, M. Zhang, P. Deshlahra, Y.-H.C. Chin, Cobalt-molybdenum oxides for effective coupling of ethane activation and carbon dioxide reduction catalysis, ACS Catal. 12 (2022) 12227–12245, https://doi.org/10.1021/acscatal.2c02525.

[32] X. Chan, N. Akter, P. Yang, C. Ooi, A. James, J.A. Boscoboinik, J.B. Parise, T. Kim, Fundamental study of furfuryl alcohol dehydration reaction over molybdenum oxide catalyst, Mol. Catal. 466 (2019) 19–25, https://doi.org/10.1016/j.mcat.2019.01.011.

[33] L. Lei, D. Huang, Y. Chen, S. Chen, R. Deng, Design of an amorphous and defect-rich CoMoOF layer as a pH-universal catalyst for the hydrogen evolution reaction, J. Mater. Chem. A. 9 (2021) 8730–8739, https://doi.org/10.1039/D1TA00505G.

[34] J. Ding, Y. Huang, Z. Liu, X. Wang, Y. Zhang, Y. Guo, R. Sheng, D. Jia, X. Tang, L. Wang, $Fe_2Mo_3O_8$/MoO_2@C composites with pseudocapacitive properties and fast diffusion kinetics for the anode of Lithium-Ion batteries, Chem. Eng. J. 431 (2022) 133984, https://doi.org/10.1016/j.cej.2021.133984.

[35] A.M. Haggar, A.E. Awadallah, A.A. Aboul-Enein, G.H. Sayed, Non-oxidative conversion of real low density polyethylene waste into hydrogen and carbon nanomaterials over MgO supported bimetallic Co-Mo catalysts with different total Co-Mo contents, Chem. Eng. Sci. 247 (2022) 117092, https://doi.org/10.1016/j.ces.2021.117092.

[36] B. Wang, B. Chen, Y. Sun, H. Xiao, X. Xu, M. Fu, J. Wu, L. Chen, D. Ye, Effects of dielectric barrier discharge plasma on the catalytic activity of Pt/CeO_2 catalysts, Appl. Catal. B Environ. 238 (2018) 328–338, https://doi.org/10.1016/j.apcatb.2018.07.044.

[37] R. Nava, B. Pawelec, P. Castaño, M.C. Álvarez-Galván, C.V. Loricera, J.L.G. Fierro, Upgrading of bio-liquids on different mesoporous silica-supported CoMo catalysts, Appl. Catal. B Environ. 92 (2009) 154–167, https://doi.org/10.1016/j.apcatb.2009.07.014.

[38] C. Ranga, R. Lødeng, V.I. Alexiadis, T. Rajkhowa, H. Bjørkan, S. Chytil, I. H. Svenum, J. Walmsley, C. Detavernier, H. Poelman, P. Van Der Voort, J. W. Thybaut, Effect of composition and preparation of supported MoO_3 catalysts for anisole hydrodeoxygenation, Chem. Eng. J. 335 (2018) 120–132, https://doi.org/10.1016/j.cej.2017.10.090.
[39] J. Jang, J.H. Ku, S.M. Oh, T. Yoon, Co-activated conversion reaction of MoO_2: $CoMoO_3$ as a negative electrode material for lithium-ion batteries, ACS Appl. Mater. Interfaces 13 (2021) 9814–9819, https://doi.org/10.1021/acsami.0c19894.
[40] W. Zhong, M. Liu, J. Dai, J. Yang, L. Mao, D. Yin, Synergistic hollow CoMo oxide dual catalysis for tandem oxygen transfer: preferred aerobic epoxidation of cyclohexene to 1,2-epoxycyclohexane, Appl. Catal. B Environ. 225 (2018) 180–196, https://doi.org/10.1016/j.apcatb.2017.11.074.
[41] W. Yu, Z. Chen, Y. Fu, W. Xiao, T. Ma, B. Dong, Y. Chai, Z. Wu, L. Wang, Co-Mo microcolumns decorated with trace Pt for large current density hydrogen generation in alkaline seawater, Appl. Catal. B Environ. 317 (2022) 121762, https://doi.org/10.1016/j.apcatb.2022.121762.
[42] A. Tuxen, S. Carenco, M. Chintapalli, C.-H. Chuang, C. Escudero, E. Pach, P. Jiang, F. Borondics, B. Beberwyck, A.P. Alivisatos, G. Thornton, W.F. Pong, J. Guo, R. Perez, F. Besenbacher, M. Salmeron, Size-dependent dissociation of carbon monoxide on cobalt nanoparticles, J. Am. Chem. Soc. 135 (2013) 2273–2278, https://doi.org/10.1021/ja3105889.
[43] A. Li, D. Yao, Y. Yang, W. Yang, Z. Li, J. Lv, S. Huang, Y. Wang, X. Ma, Active Cu^0–$Cu^{\sigma+}$ sites for the Hydrogenation of Carbon–Oxygen Bonds over Cu/CeO_2 Catalysts, ACS Catal. 12 (2022) 1315–1325, https://doi.org/10.1021/acscatal.1c04504.
[44] Z. Wang, J. Chen, E. Song, N. Wang, J. Dong, X. Zhang, P.M. Ajayan, W. Yao, C. Wang, J. Liu, J. Shen, M. Ye, Manipulation on active electronic states of metastable phase β-$NiMoO_4$ for large current density hydrogen evolution, Nat. Commun. 12 (2021) 5960, https://doi.org/10.1038/s41467-021-26256-1.
[45] M.A. Mushtaq, A. Kumar, G. Yasin, M. Arif, M. Tabish, S. Ibraheem, X. Cai, W. Ye, X. Fang, A. Saad, J. Zhao, S. Ji, D. Yan, 3D interconnected porous Mo-doped WO_3@CdS hieriarchical hollow heterostructures for efficient photoelectrochemical nitrogen reduction to ammonia, Appl. Catal. B Environ. 317 (2022) 121711, https://doi.org/10.1016/j.apcatb.2022.121711.
[46] J. Xu, C. Zhang, H. Liu, J. Sun, R. Xie, Y. Qiu, F. Lv, Y. Liu, L. Zhuo, X. Liu, J. Luo, Amorphous MoO_x-Stabilized single platinum atoms with ultrahigh mass activity for acidic hydrogen evolution, Nano Energy 70 (2020) 104529, https://doi.org/10.1016/j.nanoen.2020.104529.
[47] H. Yu, W. Wang, Q. Mao, K. Deng, Z. Wang, Y. Xu, X. Li, H. Wang, L. Wang, Pt single atom captured by oxygen vacancy-rich NiCo layered double hydroxides for coupling hydrogen evolution with selective oxidation of glycerol to formate, Appl. Catal. B Environ. 330 (2023) 122617, https://doi.org/10.1016/j.apcatb.2023.122617.
[48] G. Meng, W. Lan, L. Zhang, S. Wang, T. Zhang, S. Zhang, M. Xu, Y. Wang, J. Zhang, F. Yue, Y. Wu, D. Wang, Synergy of Single Atoms and Lewis acid sites for efficient and selective lignin disassembly into monolignol derivatives, J. Am. Chem. Soc. 145 (2023) 12884–12893, https://doi.org/10.1021/jacs.3c04028.
[49] W. Gao, S. Liu, G. Sun, C. Zhang, Y. Pan, Single-atom catalysts for hydrogen activation, Small 19 (2023) 2300956, https://doi.org/10.1002/smll.202300956.
[50] Z. Zhang, Y. Zhu, H. Asakura, B. Zhang, J. Zhang, M. Zhou, Y. Han, T. Tanaka, A. Wang, T. Zhang, N. Yan, Thermally stable single atom Pt/m-Al_2O_3 for selective hydrogenation and CO oxidation, Nat. Commun. 8 (2017) 16100, https://doi.org/10.1038/ncomms16100.
[51] Y. Ren, Y. Tang, L. Zhang, X. Liu, L. Li, S. Miao, D. Sheng Su, A. Wang, J. Li, T. Zhang, Unraveling the coordination structure-performance relationship in Pt_1/Fe_2O_3 single-atom catalyst, Nat. Commun. 10 (2019) 4500, https://doi.org/10.1038/s41467-019-12459-0.
[52] W. Gao, Z. Zhang, M. Dou, F. Wang, Highly dispersed and crystalline Ta_2O_5 anchored Pt electrocatalyst with improved activity and durability toward oxygen reduction: promotion by atomic-scale Pt–Ta_2O_5 interactions, ACS Catal. 9 (2019) 3278–3288, https://doi.org/10.1021/acscatal.8b04505.
[53] Y. Zhang, F. Zhang, L. Li, H. Qi, Z. Yu, X. Liu, C. Cao, F. Liu, A. Wang, T. Zhang, Decoration of Ru nanoparticles with mononuclear MoO_x boosts the hydrodeoxygenation of amides to amines, J. Catal. 417 (2023) 301–313, https://doi.org/10.1016/j.jcat.2022.12.012.
[54] D. Cao, K. Ye, O.A. Moses, W. Xu, D. Liu, P. Song, C. Wu, C. Wang, S. Ding, S. Chen, B. Ge, J. Jiang, L. Song, Engineering the in-plane structure of metallic phase molybdenum disulfide via Co and O dopants toward efficient alkaline hydrogen evolution, ACS Nano 13 (2019) 11733–11740, https://doi.org/10.1021/acsnano.9b05714.
[55] M. Shetty, K. Murugappan, T. Prasomsri, W.H. Green, Y. Román-Leshkov, Reactivity and stability investigation of supported molybdenum oxide catalysts for the hydrodeoxygenation (HDO) of m-cresol, J. Catal. 331 (2015) 86–97, https://doi.org/10.1016/j.jcat.2015.07.034.
[56] A.C. D'Orazio, T. Marshall, T. Sultana, J.K. Gerardi, C.U. Segre, J.P. Carlo, B. C. Eigenbrodt, High temperature X-ray absorption spectroscopy of the local electronic structure and oxide vacancy formation in the $Sr_2Fe_{1.5}Mo_{0.5}O_{6-\delta}$ solid oxide fuel cell anode catalyst, ACS Appl. Energy Mater. 2 (2019) 3061–3070, https://doi.org/10.1021/acsaem.8b01579.
[57] A.S. Asundi, A.S. Hoffman, P. Bothra, A. Boubnov, F.D. Vila, N. Yang, J.A. Singh, L. Zeng, J.A. Raiford, F. Abild-Pedersen, S.R. Bare, S.F. Bent, Understanding structure–property relationships of MoO_3-promoted Rh catalysts for syngas conversion to alcohols, J. Am. Chem. Soc. 141 (2019) 19655–19668, https://doi.org/10.1021/jacs.9b07460.
[58] D. Nicosia, R. Prins, The effect of glycol on phosphate-doped CoMo/Al_2O_3 hydrotreating catalysts, J. Catal. 229 (2005) 424–438, https://doi.org/10.1016/j.jcat.2004.11.014.
[59] Y. Chen, Y. Lu, Z. Guan, S. Liu, C. Feng, G. Sun, J. Liang, Y. Pan, C. Liu, Y. Liu, Ultrafine Co-MoS_2 monolayer catalyst derived from oil-soluble single-molecule polyoxometalates for slurry phase hydrocracking, Fuel 315 (2022) 123134, https://doi.org/10.1016/j.fuel.2022.123134.
[60] H. Liu, C. Gao, J. Chen, J. Mi, S. Yang, D. Chen, W. Si, Y. Peng, C. Sun, J. Li, Optimized local geometry and electronic structure of MoO_3/CeO_2 catalyst by adding copper cations for boosted nitrogen oxide reduction performance, Appl. Catal. B Environ. 332 (2023) 122742, https://doi.org/10.1016/j.apcatb.2023.122742.
[61] R.G. Kurniawan, N. Karanwal, J. Park, D. Verma, S.K. Kwak, S.K. Kim, J. Kim, Direct conversion of furfural to 1,5-pentanediol over a nickel–cobalt oxide–alumina trimetallic catalyst, Appl. Catal. B Environ. 320 (2023) 121971, https://doi.org/10.1016/j.apcatb.2022.121971.
[62] T.M.H. Dabros, A. Gaur, D.G. Pintos, P. Sprenger, M. Høj, T.W. Hansen, F. Studt, J. Gabrielsen, J.-D. Grunwaldt, A.D. Jensen, Influence of H_2O and H_2S on the composition, activity, and stability of sulfided Mo, CoMo, and NiMo supported on $MgAl_2O_4$ for hydrodeoxygenation of ethylene glycol, APPL CATAL A-GEN 551 (2018) 106–121, https://doi.org/10.1016/j.apcata.2017.12.008.
[63] B. Wang, M. Li, S. Zhang, H. Wu, Y. Liao, H. Li, Synergistic effect between Co single atoms and nanoparticles enables selective synthesis of bio-based benzimidazoles, Appl. Catal. B Environ. 327 (2023) 122454, https://doi.org/10.1016/j.apcatb.2023.122454.
[64] Z. Shi, F. Dong, Z. Tang, X. Dong, Design Sr, Mn-doped 3DOM $LaCoO_3$ perovskite catalysts with excellent SO_2 resistance for benzene catalytic combustion, Chem. Eng. J. 473 (2023) 145476, https://doi.org/10.1016/j.cej.2023.145476.
[65] K. Jaroszewska, A. Masalska, D. Marek, J.R. Grzechowiak, A. Zemska, Effect of support composition on the activity of Pt and PtMo catalysts in the conversion of n-hexadecane, Catal. Today 223 (2014) 76–86, https://doi.org/10.1016/j.cattod.2013.07.010.
[66] C. Liu, Q. Wei, Y. Zhou, X. Liu, K. Deng, W. Huang, H. Liu, Z. Yu, A study on the role of Ti/Si atomic ratios in the hydrodenitrogenation activity of NiMo/TiO_2-SiO_2 catalyst, Fuel 338 (2023) 126922, https://doi.org/10.1016/j.fuel.2022.126922.
[67] P. Lanzafame, K. Barbera, S. Perathoner, G. Centi, A. Aloise, M. Migliori, A. Macario, J.B. Nagy, G. Giordano, The role of acid sites induced by defects in the etherification of HMF on Silicalite-1 catalysts, J. Catal. 330 (2015) 558–568, https://doi.org/10.1016/j.jcat.2015.07.028.
[68] Y. Wang, G. Wang, L.I. Wal, K. Cheng, Q. Zhang, K.P. Jong, Y. Wang, Visualizing element migration over bifunctional metal-zeolite catalysts and its impact on catalysis, Angew. Chem. Int. Ed. 60 (2021) 17735–17743, https://doi.org/10.1002/anie.202107264.
[69] A. Saraeian, S.J. Burkhow, D. Jing, E.A. Smith, B.H. Shanks, Catalyst property effects on product distribution during the hydrodeoxygenation of lignin pyrolysis vapors over MoO_3/γ-Al_2O_3, ACS Sustain. Chem. Eng. 9 (2021) 6685–6696, https://doi.org/10.1021/acssuschemeng.1c00295.
[70] H. Ge, Y. Kuwahara, K. Kusu, Z. Bian, H. Yamashita, Ru/H_xMoO_{3-y} with plasmonic effect for boosting photothermal catalytic CO_2 methanation, Appl. Catal. B Environ. 317 (2022) 121734, https://doi.org/10.1016/j.apcatb.2022.121734.
[71] T. Qi, M.-F. He, L.-F. Zhu, Y.-J. Lyu, H.-Q. Yang, C.-W. Hu, Cooperative catalytic performance of Lewis and Brønsted acids from $AlCl_3$ salt in aqueous solution toward glucose-to-fructose isomerization, J. Phys. Chem. C. 123 (2019) 4879–4891, https://doi.org/10.1021/acs.jpcc.8b11773.
[72] G. Li, E.A. Pidko, E.J.M. Hensen, A periodic DFT study of glucose to fructose isomerization on tungstite ($WO_3 \cdot H_2O$): influence of group IV–VI dopants and cooperativity with hydroxyl groups, ACS Catal. 6 (2016) 4162–4169, https://doi.org/10.1021/acscatal.6b00869.
[73] L. Qi, Y. Zhang, M.A. Conrad, C.K. Russell, J. Miller, A.T. Bell, Ethanol conversion to butadiene over isolated zinc and yttrium sites grafted onto dealuminated beta zeolite, J. Am. Chem. Soc. 142 (2020) 14674–14687, https://doi.org/10.1021/jacs.0c06906.
[74] T. Song, Y. Qi, A. Jia, N. Ta, J. Lu, P. Wu, X. Li, Continuous hydrogenation of CO_2-derived ethylene carbonate to methanol and ethylene glycol at Cu-MoO_x interface with a low H_2/ester ratio, J. Catal. 399 (2021) 98–110, https://doi.org/10.1016/j.jcat.2021.05.004.
[75] H. Mou, Q. Chang, Z. Xie, S. Hwang, S. Kattel, J.G. Chen, Enhancing glycerol electrooxidation from synergistic interactions of platinum and transition metal carbides, Appl. Catal. B Environ. 316 (2022) 121648, https://doi.org/10.1016/j.apcatb.2022.121648.
[76] J.-L. Lin, J. Ren, N. Tian, Z.-Y. Zhou, S.-G. Sun, In situ FTIR spectroscopic studies of ethylene glycol electrooxidation on Pd electrode in alkaline solution: the effects of concentration, J. Electroanal. Chem. 688 (2013) 165–171, https://doi.org/10.1016/j.jelechem.2012.08.027.
[77] W. Xu, Z. Liu, A.C. Johnston-Peck, S.D. Senanayake, G. Zhou, D. Stacchiola, E. A. Stach, J.A. Rodriguez, Steam reforming of ethanol on Ni/CeO_2: reaction pathway and interaction between Ni and the CeO_2 support, ACS Catal. 3 (2013) 975–984, https://doi.org/10.1021/cs4000969.
[78] M. Iwamoto, M. Tanaka, S. Hirakawa, S. Mizuno, M. Kurosawa, Pulse and IR study on the reaction pathways for the conversion of ethanol to propene over scandium-loaded indium oxide catalysts, ACS Catal. 4 (2014) 3463–3469, https://doi.org/10.1021/cs5006822.